



Institut für Thermische Strömungsmaschinen
Prof. Dr.-Ing. H.-J. Bauer, Ord.

Experimental Investigation into Optimal Particle Image Velocimetry Parameters for a Centrifugal Fan

Bachelor Thesis

Carlos Durán Cañas

Supervisor: **Matthias Probst, M.Sc.**

April 2021

I hereby certify that this thesis has been composed by me and is based on my own work, unless stated otherwise. No other person's work has been used without due acknowledgment in this thesis. All references and verbatim extracts have been quoted, and all sources of information, including graphs and data sets, have been specifically acknowledged.

Karlsruhe, April 1, 2021

Contents

List of Symbols	iii
List of Figures	v
List of Tables	ix
1 Introduction	1
1.1 Motivation	1
1.2 Objective	1
1.3 Particle Image Velocimetry for Fluid Machines	1
2 Theoretical Background	3
2.1 Basic Principles of Fluid Machines	3
2.1.1 Conservation Equations	3
2.1.2 Velocity Triangle	4
2.1.3 Characteristic Curve	6
2.2 Particle Image Velocimetry	8
2.2.1 Image Acquisition	8
2.2.2 Image Evaluation	12
2.2.3 Uncertainty Estimation	14
3 Experimental Setup	17
3.1 Generic Centrifugal Fan Test Bench	17
3.2 2D2C PIV Setup	18
3.2.1 Tracer Particles	18
3.2.2 Laser and Sensor	19
3.2.3 Calibration	20
3.2.4 Region of Interest	22
3.2.5 Image Acquisition	23
3.3 PIV Evaluation	23
3.3.1 Velocity Field Analysis	23
3.3.2 Data Management	24
4 Methodology and Results	26
4.1 Influence of Interrogation Window Size	26
4.1.1 Notation, Values and Assumptions	26
4.1.2 Optimal Interrogation Window Dimensions	27
4.1.3 Validation	31
4.2 Optimal Particle Image Displacement	33
4.3 Optimal Interrogation Window Overlap	37
4.4 Optimal Cross-correlation Algorithm	42
4.5 Optimal Parameters	45

5 Conclusions and Future Work	53
References	55
Appendix	57
A.1 Optimal Image Particle Displacements for Investigated Operation Points	57
A.2 Resulting Figures for Investigated Operation Points	62

List of Symbols

Symbol	Unit	Description
<i>Latin symbols</i>		
a	m^2/s^2	Specific power
A	m^2	Area/Cross-sectional area
c	m/s	Absolute velocity
c_τ	—	System quality constant
c_{max}	mm	Maximum allowable image displacement within an interrogation window
C_f	px/mm	Conversion factor
d_p	mm	Particle diameter
d_τ	mm	Recorded image particle diameter
d_s	mm	Diffraction limited spot diameter
d_e	mm	Optical image diameter
d_r	mm	Spatial resolution for recording system
f	mm	Focal length
$f^\#$	—	Focal ratio
lp_m	$1/\text{mm}$	Image resolution
L	px	Sensor resolution
\dot{m}	kg/s	Mass flow rate
M_o	—	Magnification
M_s	Nm	Impeller mechanical torque
n	$1/\text{min}$	Rotational speed
N	—	Count
P_s	W	Electrical motor power
r	m	Radius
u	m/s	Radial velocity
\dot{V}	m^3/s	Volume flow rate
w	m/s	Relative velocity
<i>Greek symbols</i>		
ρ	kg/m^3	Density
λ	μm	Wavelength
ω	rad/s	Angular velocity
η	—	Efficiency
μ	$\text{kg}/(\text{ms})$	Dynamic viscosity
τ_p	s	Particle response time
$\sigma_{\Delta X}$	mm	Precision for a measurement
Φ	—	Interpolated/Flagged vector density
Ψ	—	Replaced vector density

Abbreviations

PIV	Particle Image Velocimetry
CFD	Computational Fluid Dynamics
2D2C PIV	2-Dimensional/2-Component Particle Image Velocimetry
VDP	Valid Detection Probability
DVR	Dynamic Velocity Range
DSR	Dynamic Spatial Range
RU	Relative Uncertainty
DEHS	Di-Ethyl-Hexyl-Sebacat
Nd:YAG	Neodymium-doped yttrium aluminum garnet
CCD	Charge-coupled device
O.P.	Operation Point

List of Figures

2.1	Relation between absolute and relative exit velocities. Image taken from Siekmann and Thamsen (2013).	4
2.2	Inlet and outlet velocity triangles for a fan impeller.	5
2.3	Characteristic curve for a fluid machine at a given rotational speed n and its facility.	6
2.4	Efficiency curve for a fluid machine.	7
2.5	Standard 2D2C PIV setup (Raffel et al. (2018)).	8
2.6	Single frame/single exposure and double frame/single exposure PIV recordings. Open circles represent the previous position for a particle. (Raffel et al. (2018))	9
2.7	Response time for different particle diameters. (Raffel et al. (2018))	10
2.8	Examples for different seeding densities.	10
2.9	Aberrations as a result of out-of-sync and out-of-focus imaging. Ideal imaging included on the top left as a reference. (Raffel et al. (2018))	12
2.10	Overlap comparison for interrogation windows.	13
2.11	Error due to incorrect installation for the camera and laser sheet. (Raffel et al. (2018))	14
2.12	Vector detection probability (VDP) as a function of the effective number of particle images inside an interrogation window. Solid lines represent the probability for having at least a given number of particle images in the interrogation window. (Raffel et al. (2018))	16
3.1	Closed loop facility. (Pritz et al. (2018))	17
3.2	Powertrain and centrifugal fan in volute casing.	18
3.3	DEHS tank with atomizer.	19
3.4	Laser/Camera assembly used during the investigation. The laser sitting on the motorized traverse can be seen on the left and the camera attached to the laser and traverse via aluminum bars can be seen on the right.	20
3.5	Previous and current calibration devices, respectively.	21
3.6	Target image for a 35mm lens. Reference point is circled for clarity.	22
3.7	Region of interest inside spiral casing. Global coordinate system is described by the figure axes.	22
3.8	Sample image with undesired reflections (left), background for the image extracted with the background removal script (middle), manually designed mask for high reflection area exclusion (right)	24
4.1	$DVR \cdot DSR$ limit for different interrogation window dimensions normalized by the maximum value.	31
4.2	Dynamic Velocity Range and Dynamic Spatial Range ratio.	32
4.3	Optimal interrogation window dimensions for 14x28 pixels, normalized by the maximum value.	32

4.4	Average pixel displacements in vertical and horizontal directions for different volume flow rates. $C_f = 13.88 \text{ px/mm}$	33
4.5	Overall quality indicators for a given operation point with varying pixel displacements. Vertical and horizontal displacements resulting in the maximum achievable $DVR \cdot DSR / DVR - DSR $ ratio are marked as optimal.	34
4.6	Individual quality indicators for a given operation point with varying pixel displacements. Vertical and horizontal displacements resulting in the maximum achievable $DVR \cdot DSR / DVR - DSR $ ratio are marked as optimal.	35
4.7	Required exposure time delay for a given target particle image displacement with respect to volume flow rate. Calculated values are plotted alongside experimental results with errors (black scatters). Extrapolated values for the target particle image displacement based on experimental results are plotted as well with a best fitting curve (red crosses and dotted line).	36
4.8	Active vectors for PIV evaluations using a multi-pass algorithm.	37
4.9	Valid vectors for PIV evaluations using a multi-pass algorithm.	38
4.10	Valid detection probability for PIV evaluations using a multi-pass algorithm. . .	39
4.11	Interpolated vectors for PIV evaluations using a multi-pass algorithm.	39
4.12	Replaced vectors for PIV evaluations using a multi-pass algorithm.	40
4.15	Valid detection probability for PIV evaluations.	42
4.16	Flagged vector count ratio.	43
4.17	Flagged vector density ratio.	43
4.18	Histogram for velocity components for optimal (top) and standard (bottom) evaluations.	47
4.19	Valid detection probabilities (VDP) for optimal and standard evaluations. . . .	47
4.20	Displacement scatter plots (left) and relative uncertainties (right) for optimal and standard evaluations.	48
4.21	Contour plots for the absolute velocities in m/s inside the area of interest in the spiral casing for the optimal evaluation (left) and standard evaluation (right). . .	49
4.22	Contour plots for the absolute velocities in m/s for the optimal evaluation (left) and standard evaluation (right). White spaces represent masked areas.	49
4.23	Valid detection probabilities (VDP) for additional (blue triangles) and calculated optimal (orange squares) evaluations.	51
4.24	Resulting average valid detection probabilities for standard (orange triangles) and calculated optimal (blue crosses) evaluations with a best fitting curve. Additional resulting VDPs for evaluations run for operation points not satisfying the desirable VDP range are plotted as well (red squares).	52
A.1	Quality indicators for a given operation point with varying pixel displacements. Vertical and horizontal displacements resulting in the maximum achievable $DVR \cdot DSR / DVR - DSR $ ratio are marked as optimal.	57
A.2	Individual quality indicators for a given operation point with varying pixel displacements. Vertical and horizontal displacements resulting in the maximum achievable $DVR \cdot DSR / DVR - DSR $ ratio are marked as optimal.	57

A.3	Quality indicators for a given operation point with varying pixel displacements. Vertical and horizontal displacements resulting in the maximum achievable $DVR \cdot DSR / DVR - DSR $ ratio are marked as optimal.	58
A.4	Individual quality indicators for a given operation point with varying pixel displacements. Vertical and horizontal displacements resulting in the maximum achievable $DVR \cdot DSR / DVR - DSR $ ratio are marked as optimal.	58
A.5	Quality indicators for a given operation point with varying pixel displacements. Vertical and horizontal displacements resulting in the maximum achievable $DVR \cdot DSR / DVR - DSR $ ratio are marked as optimal.	59
A.6	Individual quality indicators for a given operation point with varying pixel displacements. Vertical and horizontal displacements resulting in the maximum achievable $DVR \cdot DSR / DVR - DSR $ ratio are marked as optimal.	59
A.7	Quality indicators for a given operation point with varying pixel displacements. Vertical and horizontal displacements resulting in the maximum achievable $DVR \cdot DSR / DVR - DSR $ ratio are marked as optimal.	60
A.8	Individual quality indicators for a given operation point with varying pixel displacements. Vertical and horizontal displacements resulting in the maximum achievable $DVR \cdot DSR / DVR - DSR $ ratio are marked as optimal.	60
A.9	Quality indicators for a given operation point with varying pixel displacements. Vertical and horizontal displacements resulting in the maximum achievable $DVR \cdot DSR / DVR - DSR $ ratio are marked as optimal.	61
A.10	Individual quality indicators for a given operation point with varying pixel displacements. Vertical and horizontal displacements resulting in the maximum achievable $DVR \cdot DSR / DVR - DSR $ ratio are marked as optimal.	61
A.11	Histogram for velocity components for optimal and standard evaluations.	62
A.12	Valid detection probabilities (VDP) for optimal and standard evaluations.	62
A.13	Displacement scatter plots (left) and relative uncertainties (right) for optimal and standard evaluations.	63
A.14	Contour plots inside the area of interest in the spiral casing for the optimal evaluation (left) and standard evaluation (right).	63
A.15	Contour plots for the optimal evaluation (left) and standard evaluation (right). White spaces represent masked areas.	64
A.16	Histogram for velocity components for optimal and standard evaluations.	64
A.17	Valid detection probabilities (VDP) for optimal and standard evaluations.	65
A.18	Displacement scatter plots (left) and relative uncertainties (right) for optimal and standard evaluations.	65
A.19	Contour plots inside the area of interest in the spiral casing for the optimal evaluation (left) and standard evaluation (right).	66
A.20	Contour plots for the optimal evaluation (left) and standard evaluation (right). White spaces represent masked areas.	66
A.21	Histogram for velocity components for optimal and standard evaluations.	67
A.22	Valid detection probabilities (VDP) for optimal and standard evaluations.	67

A.23 Displacement scatter plots (left) and relative uncertainties (right) for optimal and standard evaluations.	68
A.24 Contour plots inside the area of interest in the spiral casing for the optimal evaluation (left) and standard evaluation (right).	68
A.25 Contour plots for the optimal evaluation (left) and standard evaluation (right). White spaces represent masked areas.	69
A.26 Histogram for velocity components for optimal and standard evaluations.	69
A.27 Contour plots inside the area of interest in the spiral casing for the optimal evaluation (left) and standard evaluation (right).	70
A.28 Contour plots for the optimal evaluation (left) and standard evaluation (right). White spaces represent masked areas.	70
A.29 Histogram for velocity components for optimal and standard evaluations.	71
A.30 Valid detection probabilities (VDP) for optimal and standard evaluations.	71
A.31 Displacement scatter plots (left) and relative uncertainties (right) for optimal and standard evaluations.	72
A.32 Contour plots inside the area of interest in the spiral casing for the optimal evaluation (left) and standard evaluation (right).	72
A.33 Contour plots for the optimal evaluation (left) and standard evaluation (right). White spaces represent masked areas.	73

List of Tables

3.1	Facility and impeller specifications. (Feldle (2018))	18
3.2	Specifications for the sensor used.	20
4.1	Operation point parameters. Impeller was attempted to be kept at 600 rpm.	34
4.2	Optimal average pixel displacements for investigated operation points.	35
4.3	Average interpolated and replaced vector density ratios with respect to results using a 0% overlap.	41
4.4	Average flagged vector density ratios with respect to the single pass algorithm.. .	44
4.5	Optimal acquisition parameters for multiple operation points, rounded to the closest integer.	45
4.6	Optimal interrogation window dimensions for a multi-grid algorithm using a 50% overlap. Dimensions are doubled due to the use of a 50% overlap.	45
4.7	Dynamic velocity and spatial range values and ratios for optimal and standard evaluations.	46
4.8	Final comparisons for optimal and standard evaluations for all investigated operation points.	50
4.9	Additional evaluation results for O.P.'s 0 and 5.	51

1 Introduction

1.1 Motivation

Nowadays, an increasing number of engineers rely on simulated data to make decisions for their designs. These techniques allow the user to investigate multiple configurations of their intended product and compare their performances without having to invest in multiple prototypes. In the field of fluid machinery, the simulation technique of Computational Fluid Dynamics (CFD) is widely used to understand the internal flows for a given design. This technique has been improved to the point where many designers base their products solely on CFD results.

Although widely accepted, these simulation results are based on assumptions and simplifications that can sometimes lead to erroneous solutions, therefore they must be compared to real world experimental data whenever possible to validate their accuracy. A common technique used to provide experimental data for this validation is Particle Image Velocimetry (PIV).

In order to properly compare simulated and experimental data, an exhaustive attention should be given to the reduction of uncertainty in the results yet, it is common practice throughout literature that PIV results are assumed to be accurate with no particular attention to their validity. Due to its experimental nature, PIV is susceptible to inaccuracies caused by human error. These uncertainties are influenced by multiple parameters regarding the acquisition and evaluation processes. Therefore, a proper procedure should be followed to reduce this uncertainty and guarantee repeatability for the experiment.

1.2 Objective

The objective of this thesis is the investigation for the experimental technique of Particle Image Velocimetry and the accuracy of its results. This is done through the examination for the methodology required to obtain optimal acquisition and evaluation parameters. For this, the context of a generic centrifugal fan test bench with the aim of providing validation data for numerical simulations is used. Acquisition parameters such as the optimal average image particle displacement and time delay between exposures are thoroughly investigated alongside evaluation parameters such as interrogation window dimensions, sample overlap and cross-correlation algorithms. An extensive investigation into the velocity flow fields inside the spiral casing for a centrifugal fan is carried out using different setup and parameter configurations with the goal of comparing the resulting quality for the measurements.

1.3 Particle Image Velocimetry for Fluid Machines

Multiple works regarding the use of Particle Image Velocimetry as an investigation tool for velocity fields in turbomachinery already exist, with the most notable studies being on centrifugal fans and pumps. These studies focus mainly on the test subject, while PIV is purely utilized as

a measurement tool. In most cases, basic parameters are used and the validity for their results is not questioned.

I.C. Shepherd and R.F. La Fontaine examined the velocity field inside a centrifugal fan housing by means of 2D2C PIV to determine flow structures which affect the blade-passing tone (BPT). This was done with the goal of reducing the blade-passing noise caused by the impeller. PIV evaluations for exposures captured with a 35mm lens were run with a 33×23 px interrogation window size. The reasoning behind this choice as well as the validity of the resulting velocity fields were not discussed, which in this case are of large importance since measurements were carried out near the impeller blades and the volute cutoff. These regions are characterized by high turbulence and velocity fluctuations as well as high reflections from the nearby surfaces, both being contributing factors towards the impairment of the accuracy for a PIV measurement. (Shepherd and La Fontaine (1993))

J.H. Yoon and S.J. Lee examined the flow field behind a low speed, forward-swept axial fan by means of stereoscopic PIV (SPIV). This was done with the goal of validating numerical predictions and understanding the flow structure in the design process of axial fans. The areas for local maximum velocities were identified for the fan flow. In their work, it is stated that the an exposure time delay of $1 \mu s$ was used based on the blade angle. Evaluations were run with settings predetermined by the manufacturer for the equipment used, which suggests that results are relatively valid while their quality could still have room for improvement. Once more, the accuracy for their results is not stated, therefore an assessment of their validity cannot be made. (Yoon and Lee (2004))

J. Keller investigated the rotor-stator interactions induced pressure fluctuations and flow structures in a centrifugal pump. For this, a construction of a transparent pump with a 2-D impeller was carried out in order to measure the velocity fields in the volute tongue region. These PIV measurements included the application of stereo PIV in a 2D3C setup in order to measure all three velocity components. For the in-plane evaluations, a multi-grid algorithm starting at 64×64 pixels and ending at 32×32 pixels was used to increase the computational cost required. (Keller (2014))

2 Theoretical Background

With the intention of providing a better comprehension for the topics discussed throughout this work, this chapter presents the required basics. The topic of fluid machinery is discussed first. Basic equations and diagrams regarding the behavior of fluids in turbomachinery and the laws and assumptions applicable to this work are discussed in detail. The topic of particle image velocimetry (PIV) is then discussed. A description for a PIV procedure is given alongside a thorough discussion on the different required processes. The components involved during these processes as well as their effects on the final results are additionally inspected.

2.1 Basic Principles of Fluid Machines

Fluid machines deal with the transformation of fluid flow energy into mechanical energy (or vice versa) in a continuous mode of operation. This flow can be liquid or gaseous. On the other hand, displacement machines deal with the transfer of mechanical energy between components in an oscillating fashion. Fluid machines can further be divided into hydraulic fluid machines and thermal fluid machines depending on the specific compression ratio. In general, the compression ratio between the inlet and outlet positions (p_2/p_1) must be below 1.3 for a fluid machine to qualify as a hydraulic fluid machine. For this work, a centrifugal fan was investigated. The flow inside the fan was assumed to be adiabatic and quasi-incompressible¹, therefore the centrifugal fan at hand qualifies as a hydraulic fluid machine.

2.1.1 Conservation Equations

In the field of fluid mechanics, the stream filament theory is used to describe the behavior of a fluid flow. The flow is described as a bundle of stream lines on which properties are constant throughout the stream tube cross-sectional area and only vary in the direction of the flow. From this theory, multiple conservation equations are derived based on the simplifications it conveys. (Spurk and Aksel (2020))

The law of conservation of mass states that mass cannot be created or destroyed in a closed system. This can be formulated as:

$$\frac{dm}{dt} = \dot{m}_{in} - \dot{m}_{out} . \quad (2.1)$$

In the case of a stream tube no mass flows through the surface, therefore the mass flow rate inside the stream tube must be constant, yielding:

$$\dot{m} = \rho \bar{c} A = const. \quad (2.2)$$

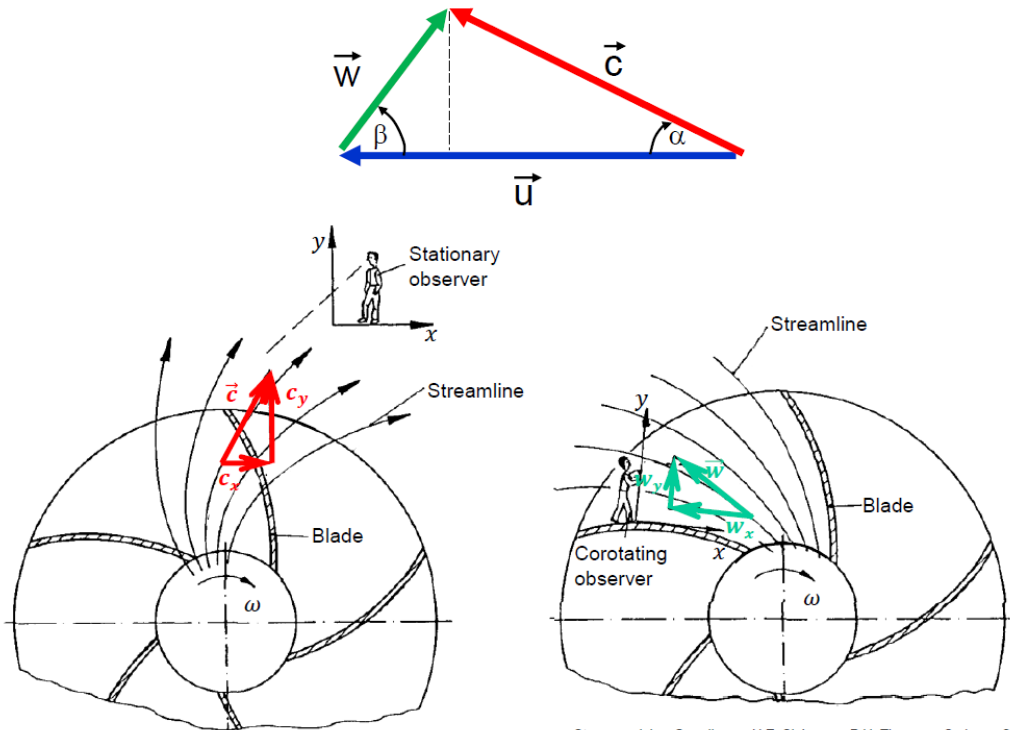
¹The average density between inlet and outlet positions is taken as the constant density.

with \dot{m} standing for the mass flow rate, ρ for the flow density, A for the cross-sectional area and \bar{c} for the mean velocity. For the case of an incompressible flow with $\rho = \text{const.}$, the volume flow rate \dot{V} for the stream tube yields:

$$\dot{V} = \bar{c}A = \text{const.} \quad (2.3)$$

2.1.2 Velocity Triangle

The most important component for a centrifugal fan is its impeller. Here, the transfer of mechanical rotational energy into fluid flow energy takes place. By means of rotation, the impeller creates a low pressure zone at the inlet, causing the fluid to be sucked into the blade channels. The fluid is then accelerated by means of transfer of momentum from the impeller blades and is then discharged into the spiral casing at a 90° angle with respect to the inlet direction. This exit velocity can vary depending on the position of the observer as seen in Figure 2.1.



Strömungslehre-Grundlagen, H.E. Siekmann, P.U. Thamsen, Springer, 2.Auflage, 2008

Figure 2.1: Relation between absolute and relative exit velocities. Image taken from Siekmann and Thamsen (2013).

With β being the relative angle between the relative and radial velocities, α the absolute angle between the absolute and radial velocities, \vec{u} the radial velocity at the outer edge of the impeller, \vec{w} the relative exit velocity from the outer blade coordinate system and \vec{c} the absolute exit velocity from a stationary global coordinate system.

This velocity triangle can be used to analyze the flow inlet and outlet velocities at the impeller, pictured in Figure 2.2.

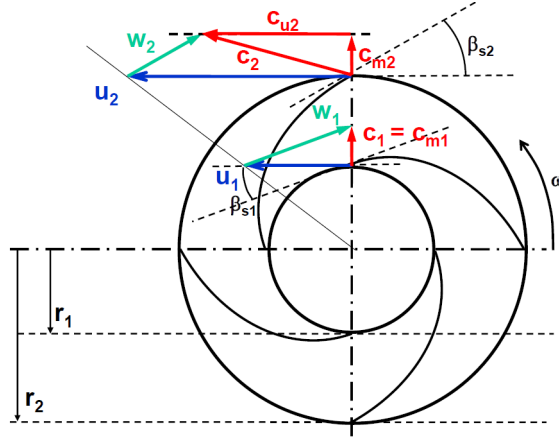


Figure 2.2: Inlet and outlet velocity triangles for a fan impeller.

With values subscripted $(\cdot)_u$ to identify circumferential directions and $(\cdot)_m$ for radial directions. From this, the power transfer between the impeller blades and the fluid can be calculated with Euler's equation. In order to derive it, the principle of angular momentum in circumferential direction must first be applied. (Siekmann and Thamsen (2013))

$$\left[\sum \vec{M}_a \right]_u = \left[\frac{d\vec{L}}{dt} \right]_u \quad (2.4)$$

Taking the impeller mechanical torque M_s as:

$$\left[\sum \vec{M}_a \right]_u = M_s = \frac{P_s}{\omega}, \quad (2.5)$$

and the angular momentum for the fluid $\left[\frac{d\vec{L}}{dt} \right]_u$ as:

$$\left[\frac{d\vec{L}}{dt} \right]_u = \int_A \rho \cdot (\vec{r} \times \vec{c}) \cdot \vec{c} \cdot \vec{n} \, dA \quad (2.6)$$

$$= - \int_{A_1} \rho r c_u c_m \, dA + \int_{A_2} \rho r c_u c_m \, dA \quad (2.7)$$

$$= \dot{m} (r_2 c_{u2} - r_1 c_{u1}), \quad (2.8)$$

it yields:

$$M_s = \dot{m} (r_2 c_{u2} - r_1 c_{u1}) = \dot{m} \Delta (rc_u). \quad (2.9)$$

Taking:

$$M_s = \frac{P_s}{\omega} \quad (2.10)$$

$$r\omega = u , \quad (2.11)$$

with ω being the impeller angular velocity, P_s the power delivered by the rotating shaft, r the impeller radius and u the impeller circumferential velocity, the specific power transfer between the impeller and the flow a_{12} results in:

$$\frac{P_s}{\dot{m}} = a_{12} = \Delta_{12}(uc_u) . \quad (2.12)$$

2.1.3 Characteristic Curve

Measuring the characteristic curve for a fluid machine is useful in order to get an understanding of the operation point being measured. Fluid machines are components for a facility, therefore the point of operation is dependent on the performance of both. A performance (or characteristic) curve can be computed for both the fluid machine and the facility. This is achieved by measuring the pressure change between the inlet and outlet positions Δp_{tot} with respect to the volume flow rate \dot{V} . The operation point can be found at the intersection for these curves since a fluid machine can only operate if its pressure change matches the pressure change for the facility.

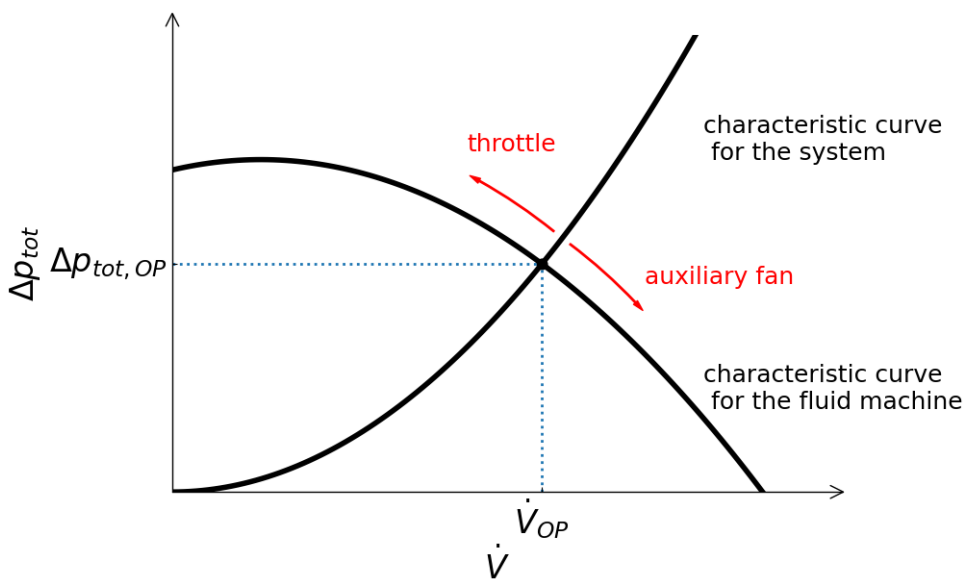


Figure 2.3: Characteristic curve for a fluid machine at a given rotational speed n and its facility.

The operation point for a fluid machine can be changed with the help of a throttle and an auxiliary fan. As depicted in figure 2.3, closing the throttle moves the operation point towards smaller volume flow rates while increasing the speed for the auxiliary fan moves the operation point to higher volume flow rates.

Additionally, the efficiency for the fan η can be calculated. The general formula to calculate it is given by:

$$\eta = \frac{P}{P_s} \quad (2.13)$$

taking P as the power gained by the fluid and P_s as the power delivered by the rotating shaft. These are given by:

$$P = \Delta p_{tot} \dot{V} \quad (2.14)$$

$$P_s = M_s \omega = M_s \cdot 2\pi n \quad (2.15)$$

resulting in:

$$\eta = \frac{\Delta p_{tot} \dot{V}}{M_s \cdot 2\pi n} \quad (2.16)$$

This calculation results in the efficiency curve for the fan which can then be plotted alongside its characteristic curve to find the operation point for maximum efficiency. An example for this is given in Figure 2.4.

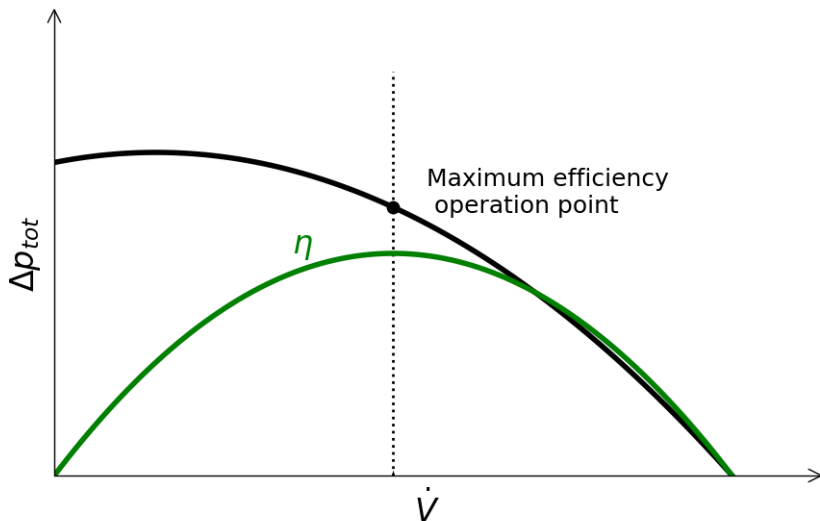


Figure 2.4: Efficiency curve for a fluid machine.

2.2 Particle Image Velocimetry

Particle Image Velocimetry is a non-intrusive optical measurement technique used to map instantaneous velocity fields in a fluid. It has been developed since the early 1980s and is now a well-established measurement technique in the fields of fluid dynamics research and mechanical engineering. In order to measure velocity fields, the fluid is injected with small tracer particles which follow the direction of the flow closely (Meinhart et al. (1999)). These particles are repeatedly illuminated by light sheets created by a rapid double-pulsed laser and image pairs are simultaneously captured by a CCD camera or photographic film with a set time in between pulses. These images are divided into interrogation windows (IW) resulting in a mesh grid for the image pair, which are investigated individually by means of a correlation algorithm. Since the time between pulses is previously known, these images are then processed to obtain the average particle displacement in between pulses for each interrogation window in order to calculate the velocity fields. (Adrian (1997), Stamhuis (2006))

For this work, a standard 2-dimensional, 2-component (2D2C) PIV setup was used following the previously stated procedure. A basic representation of a 2D2C setup can be seen in Figure 2.5.

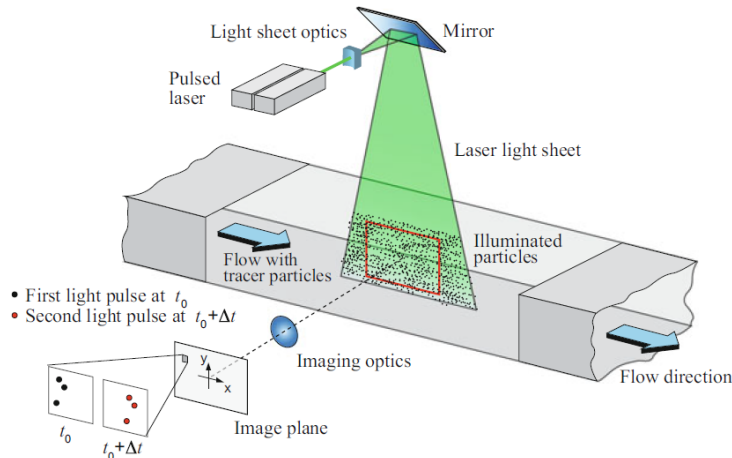


Figure 2.5: Standard 2D2C PIV setup (Raffel et al. (2018)).

Multiple setup components play an important role in the final results for a PIV measurement. These will be discussed in the following subsections.

2.2.1 Image Acquisition

For this work's procedure, a double frame/single exposure recording technique was used. This conveys that two singly exposed images are captured for every sample, resulting in a collection of double images with suffixes A and B (see section 3.3.2 for a detailed explanation on the file management). Figure 2.6 shows the difference between a single frame/single exposure and a double frame/single exposure recording.

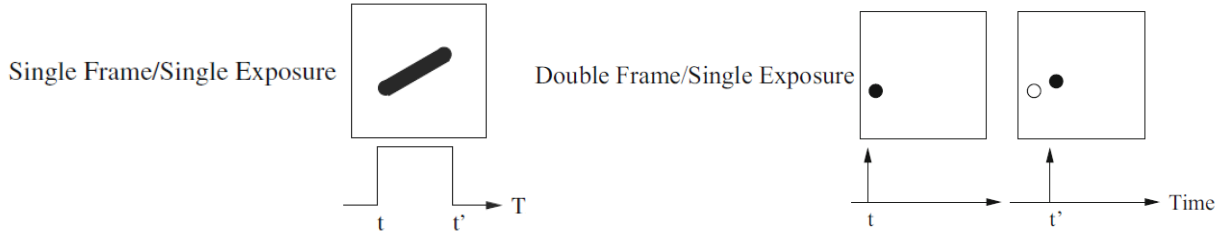


Figure 2.6: Single frame/single exposure and double frame/single exposure PIV recordings.
Open circles represent the previous position for a particle. (Raffel et al. (2018))

Tracer Particles

PIV is considered an indirect measurement technique since it calculates the velocity field for a flow by capturing the velocity field for the tracer particles injected into this flow. Therefore, the characteristics of the tracer particles being used are of high relevance for the results being measured.

A crucial tracer particle property that requires particular attention is the accuracy at which it is able to follow the direction of the flow being investigated. This accuracy is influenced primarily by the effect gravity has on the particles if the densities between the fluid ρ and the particles ρ_p do not closely match. This effect can be calculated by deriving the velocity lag of a particle in an accelerating fluid U_s derived from Stoke's drag law:

$$U_s = U_p - U = d_p^2 \frac{(\rho_p - \rho)}{18\mu} a, \quad (2.17)$$

with the particle response time:

$$\tau_p = d_p^2 \frac{\rho_p}{18\mu}, \quad (2.18)$$

with U_p and U being the velocities for the particle and the flow respectively, a the acceleration of the flow, d_p the average particle diameter and μ the dynamic viscosity for the flow. The reduction of this value can be achieved by reducing the density difference between the fluid and the tracer particles. This is easily achievable for liquid flows. In the case of gaseous flows, this difference is difficult to minimize since tracer particles are usually liquids or solids. Therefore, a reduction of the particle diameter would result in a reduction of the particle velocity lag. Figure 2.7 shows the theoretical response times for oil particles in an instantaneously decelerated flow of air for different particle diameters.

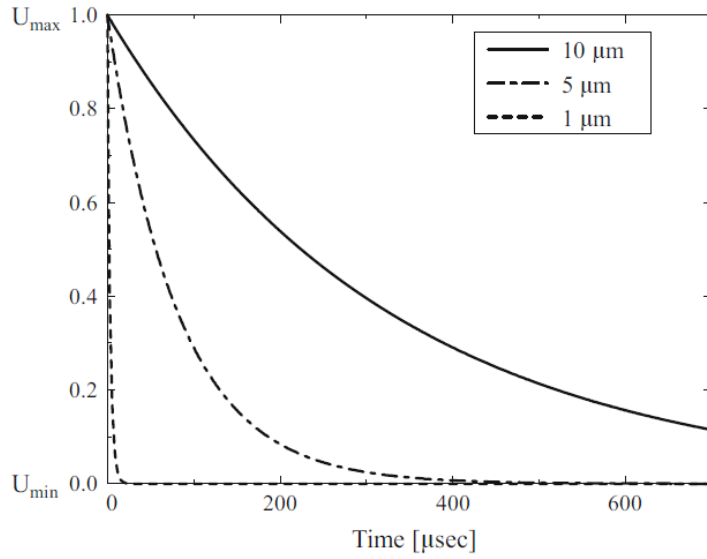


Figure 2.7: Response time for different particle diameters. (Raffel et al. (2018))

Furthermore, the concentration of tracer particles in the recorded images also plays an important role in the quality of the overall PIV measurement. Multiple ongoing investigations are being done into the quantification of the seeding density for a PIV measurement. However, this has proven to be challenging since this seeding density is hard to measure and often is dependent on the experience of the user.

If the density is too low, the tracer particle count will not be sufficient for the correlation algorithm to determine an accurate result. This could lead to missing velocity data due to particle-less interrogation windows. On the other hand, if the particle density is too high particle overlap begins to occur, causing the correlation algorithm to not be able to determine the intensity peaks accurately. Both of these situations lead to high spurious vector counts. Therefore, a balance between both should be found. Figure 2.8 shows underseeded, properly seeded and overseeded image samples respectively.

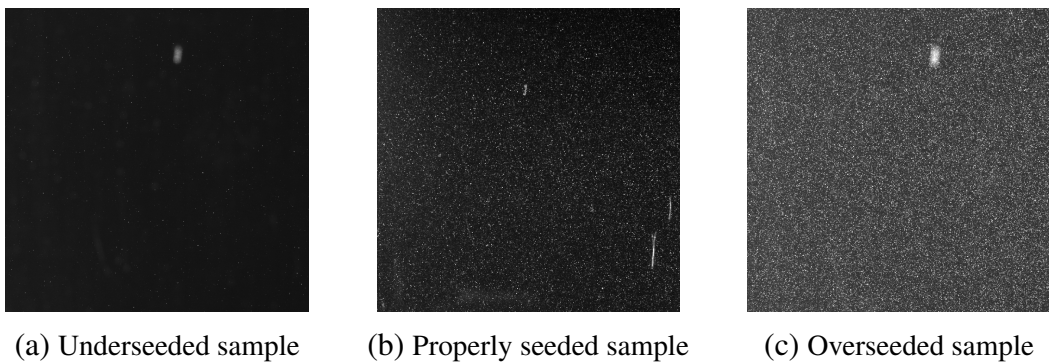


Figure 2.8: Examples for different seeding densities.

Exposure Time Delay

Owing to the fact that the calculated velocity fields are a function of the particle displacement between images and the time delay in between exposures, a careful choice for the time delay should be done. In literature, it is recommended to keep the average particle image displacement between 5 and 10 pixels, with 10 pixels being the optimal value (Hain and Kähler (2007)). This can be achieved by varying the exposure time delay for each measurement depending on the flow velocity components for a given experiment since the average particle image displacements $\overline{\Delta X}^{(px)}$ and $\overline{\Delta Y}^{(px)}$ are determined by:

$$\overline{\Delta X}^{(px)} = 1000 \cdot C_f \bar{u} \Delta t \quad (2.19)$$

$$\overline{\Delta Y}^{(px)} = 1000 \cdot C_f \bar{v} \Delta t , \quad (2.20)$$

with Δt being the time delay between consecutive exposures, C_f the conversion factor for the image in px/mm and \bar{u} and \bar{v} being the horizontal and vertical flow velocity components, respectively. A thorough investigation into the choice for exposure time delay was carried out for the setup at hand in subsection 4.1.2.

Camera Focus and Exposure

As mentioned earlier, when using PIV as a measurement technique, the velocity field for a flow is calculated by means of capturing the velocity field for the injected tracer particles. Therefore, the quality for the measurement is directly affected by the quality of the particle image acquisition. A big contributor for the quality of an experiment is the camera setup being used. This is dictated by the image sharpness which can be controlled by changing the focus and aperture for the lens. These parameters must be fine-tuned during the calibration process (see subsection 3.2.3) in order to get the best quality possible.

Image particle focus, similar to image particle density, is difficult to quantify and in most cases it is dependent on the experience of the user. Multiple examples exist in literature and are used as a guide in order to achieve a correct image particle focus. Examples for aberrations due to out-of-sync and out-of-focus imaging are given in Figure 2.9.

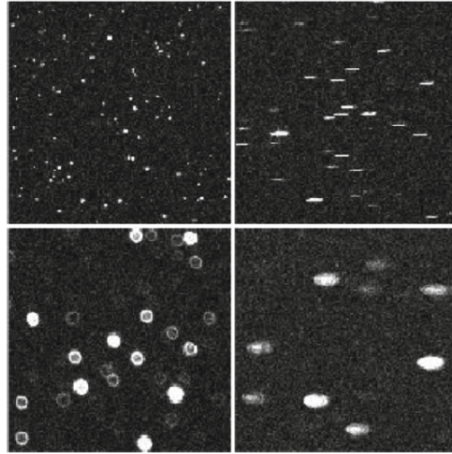


Figure 2.9: Aberrations as a result of out-of-sync and out-of-focus imaging. Ideal imaging included on the top left as a reference. (Raffel et al. (2018))

2.2.2 Image Evaluation

Following the acquisition process, images are evaluated to extract the velocity field for a given plane. This subsection explains the different components involved in the evaluation process and their effects on the final PIV evaluation results.

Interrogation Window Dimensions

As mentioned earlier, in order to extract velocity fields for a measurement, image pairs are divided into individually processed interrogation windows creating a mesh grid for the image pair. The dimensions for these interrogation windows determine the resolution for a measurement. Smaller interrogation windows increase the resolution for a measurement generally at the expense of its accuracy.

Interrogation window dimension choices for a PIV measurement are closely related to the flow characteristics and acquisition parameters. In order to choose an optimal interrogation window size, the one-quarter rule should be followed. This rule states that the displacement for a particle image should not be larger than one quarter of the interrogation window span in the trajectory of the particle image shift (Keane and Adrian (1991)). Therefore, the optimal window dimensions for a measurement $D_{I,X}$ and $D_{I,Y}$ can be calculated with:

$$D_{I,x} = 4 \cdot \overline{\Delta X}^{(px)} \quad (2.21)$$

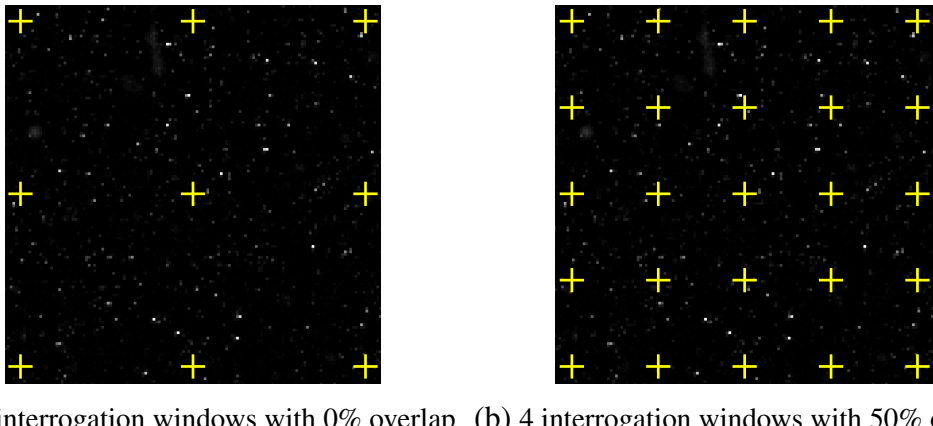
$$D_{I,y} = 4 \cdot \overline{\Delta Y}^{(px)} . \quad (2.22)$$

These dimensions are two of the factors that help determine the quality indicators for a measurement, namely its relative uncertainty (RU) and its dynamic spatial and velocity ranges (DSR and

DVR), which measure the certainty at which a measurement is able to resolve particle displacements, the resulting image resolution and the range of resolvable velocities for a given measurement, respectively. A calculation for optimal interrogation window dimensions alongside with their quality indicators for given velocity components is thoroughly explained in section 4.1.

Sample Overlap

When evaluating a PIV measurement, it is normal practice to allow a certain overlap between interrogation windows. This tool allows the comparison among adjacent interrogation windows, which results in the elimination of correlation anomalies. Adjusting the overlap for an interrogation window defines the increment at which images are sampled, determining the final interrogation grid size. Increasing the sample overlap results in a higher number of vectors since the sample size is increased. However, an excessive increase of it can lead to oversampling, meaning that the number of vectors for an evaluation is increased but there is no meaningful information being given (Meinhart et al. (1999)). Figure 2.10 shows an example for evaluations with 0% overlap and 50% overlap for the same interrogation window dimensions, respectively.



(a) 4 interrogation windows with 0% overlap (b) 4 interrogation windows with 50% overlap

Figure 2.10: Overlap comparison for interrogation windows.

Literature recommends using an overlap of 50% to maximize the spatial range for a given evaluation (Stamhuis (2006)). This overlap percentage is considered to be the best balance between information density and oversampling for a PIV evaluation. An investigation into the effect of sample overlap on flagged vectors was performed in section 4.3.

Algorithm

The way in which the correlations are applied on images for a PIV evaluation is of great importance and affects the final results. Therefore, several algorithms have been designed with different approaches to extract the displacement fields. For the setup at hand, three different correlation algorithms were available and investigated. Their methods are explained in the following.

The single pass algorithm is considered the standard due to its simple approach. When using this algorithm, the PIV interrogation is run once through the image pairs. This allows for a faster interrogation compared to the other correlation algorithms. Conversely, the multi-pass and multi-grid algorithms refine these results by running multiple interrogations on the images. However, these two vary in the way they approach this method as well. The multi-pass algorithm repeats the interrogation at least once, offsetting the sampling positions by the integer shift determined in the preceding pass. On the other hand, the multi-grid algorithm uses a coarse-to-fine pyramid approach starting with a large interrogation window which is decreased on every iteration of the interrogation until the desired final size is reached. Both of these algorithms result in a higher run time. An investigation into the quality for a measurement based on the used algorithm was done in section 4.4.

2.2.3 Uncertainty Estimation

Due to the experimental nature of this investigation, several sources of error regarding PIV have to be considered when analyzing the gathered results. This subsection details the most common PIV measurement error contributors.

Installation Errors

Errors due to incorrect installation for the camera and laser may arise for PIV measurements. These are particularly significant if a large flow component perpendicular to the laser sheet exists which may result in large perspective errors. This error increases in magnitude with increasing distance from the optical axis of the camera lens. Figure 2.11 shows an example for this.

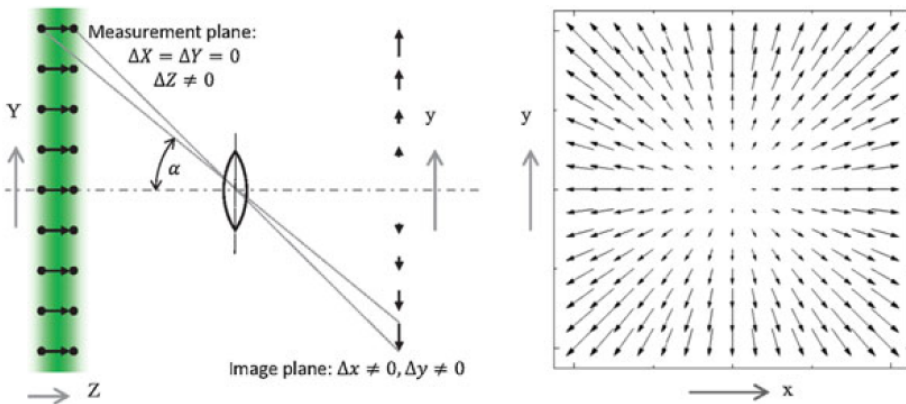


Figure 2.11: Error due to incorrect installation for the camera and laser sheet. (Raffel et al. (2018))

This error can be decreased by reducing the field of view for the image which can be done by selecting a lens with a larger focal length or by decreasing the distance between the laser sheet and the camera.

System Component Errors

Errors in this category involve system component deficiencies. Examples for this category are timing errors involving the set exposure time delay Δt and errors in the manufacturing of the used calibration grid. These errors can lead to inaccuracies during the calculation for the flow velocities and can sway the results from the real solution. In order to account for these errors, multiple images must be taken for each experiment in order to average out the results and to better identify outliers. The number of images required to reduce this error has been previously investigated by *Warner and Smith*. They concluded that, for the setup being investigated in this work, 1000-1500 images per measurement are enough in order to reduce these effects (*Warner and Smith (2014)*). This is also confirmed by plotting the mean relative standard deviation (MRSD) with respect to the number of images being considered.

Errors Due to Invalid Measurements

At its initial stages, PIV measurements were prone to large invalid vector counts due to low signal-to-noise ratios caused by low output energies for the available lasers. For this reason, a lot of effort went into the detection and removal of outliers, most commonly referred to as invalid vectors. Unlike valid vectors, outliers must be dealt with in a PIV measurement to avoid a deviation from the valid result. This is done by either excluding the vector from a measurement or interpolating values from neighboring vectors to replace the outlier. Therefore, the valid detection probability (VDP) should be always stated alongside a PIV measurement result. This is a measure for the amount of valid vectors with respect to the total number of vectors for a given measurement and it is given by:

$$VDP = \frac{N_{valid}}{N_{total}} . \quad (2.23)$$

To illustrate the VDP in dependency on the effective number of particle images in an interrogation window $N = N_I F_I F_O$, the graph in figure 2.12 is commonly used.

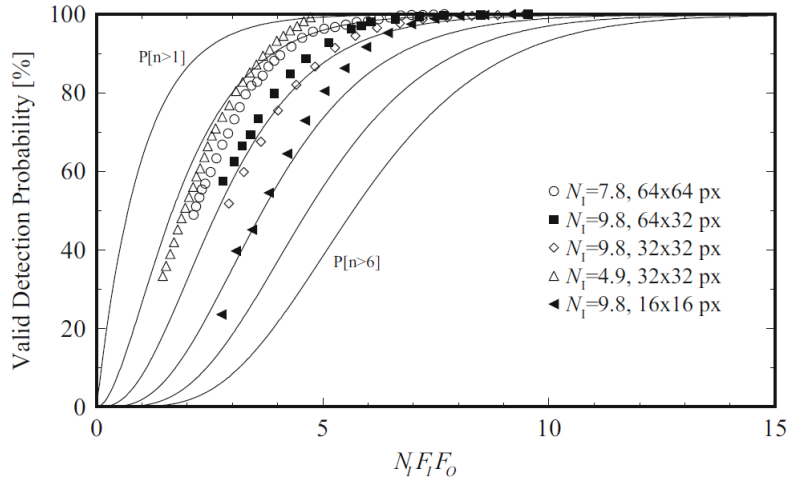


Figure 2.12: Vector detection probability (VDP) as a function of the effective number of particle images inside an interrogation window. Solid lines represent the probability for having at least a given number of particle images in the interrogation window. (Raffel et al. (2018))

Where N_l is the number of particle images within an interrogation window, F_l the in-plane loss of pairs and F_O the out-of-plane loss of pairs. F_l and F_O become zero per definition if the particle displacement is larger than the interrogation window extent (D_I) or the light sheet thickness (Δz_0). This is shown for their equations:

$$F_l = \left(1 - \frac{|\Delta x|}{D_I}\right) \left(1 - \frac{|\Delta y|}{D_I}\right) \quad (2.24)$$

$$F_O = \left(1 - \frac{|\Delta z|}{\Delta z_0}\right). \quad (2.25)$$

Generally, a VDP value of 90 to 95% is desired for a PIV measurement to be considered appropriate (Raffel et al. (2018)). Values larger than 95% are not considered undesirable but it conveys that a larger spatial resolution could be chosen. To achieve this range, the effective number of particle images N for a measurement should be at least 5 on average. This ensures a decrease in the amount of spurious measurements to a few percentage.

3 Experimental Setup

For this work, a centrifugal fan test bench was considered in order to investigate multiple PIV parameters and the effects they have on the results. This chapter illustrates the experimental setup for this test bench as well as the PIV setup used during the experiments.

3.1 Generic Centrifugal Fan Test Bench

To ensure a constant flow of tracer particles through the test object, the facility used during these experiments is designed as a closed loop made up of a model fan (MF) and a settling chamber. A schematic for the facility is shown in figure 3.1.

Due to its large volume, the velocity for the air inside the settling chamber (5) is negligible. Therefore the static pressure for the flow at this position is considered to be its total pressure. The model fan (2) being investigated is located inside a spiral casing. The impeller for the fan is powered by an electric motor (M) via a drive shaft that is connected to a measuring shaft. This ensemble is referred to as the powertrain. The impeller draws air from the inlet duct (1) and redirects it radially into the outlet duct which then passes through the volume flow measuring section (4). This calculation is carried out according to DIN EN ISO 5167. The temperatures (T) and pressure difference (Δp_{stat}) are measured for the inlet and outlet positions (3) to determine the operation point mentioned in subsection 2.1.3. The flow then returns to the settling chamber which is equipped with a throttle (7) and an auxiliary fan (6) used to control the operation point for the facility (see figure 2.3). Specifications for the components of the closed loop can be seen in table 3.1.

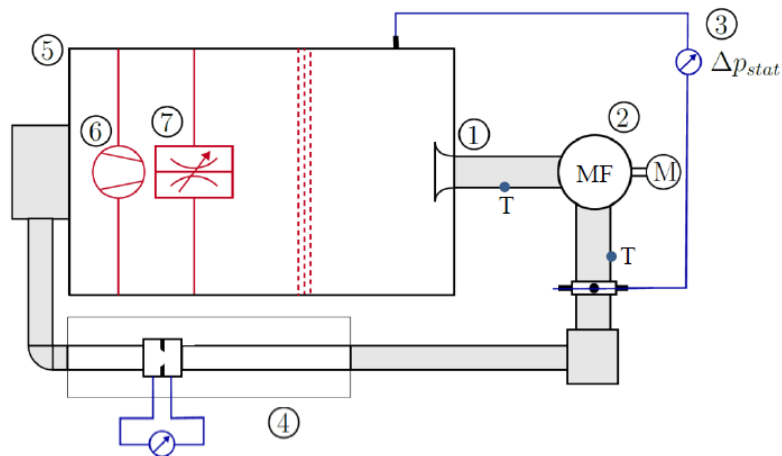


Figure 3.1: Closed loop facility. (Pritz et al. (2018))

Property	Value	Unit
Outlet duct cross-section A_{out}	0.0219	[m ²]
Impeller weight m_{imp}	2.4	[kg]
Number of impeller blades	9	[\cdot]
Impeller inlet cross-section $A_{imp,in}$	0.016	[m ²]
Impeller outlet cross-section $A_{imp,out}$	0.023	[m ²]
Impeller inlet diameter $d_{imp,in}$	0.138	[m]
Impeller outlet diameter $d_{imp,out}$	0.325	[m]

Table 3.1: Facility and impeller specifications. (Feldle (2018))

The aim of this facility is the investigation of flow structures at different positions inside the volute casing for a fast-prototyped model fan. This fan consists of a backward-curved, nine-blade, two-dimensional design manufactured with the aim of easy comparability to industrial fans and modeling for CFD simulations. The spiral casing, as well as the impeller, are constructed of acrylic glass for optical accessibility. The test bench is also equipped with pressure and temperature sensors at the inlet and outlet positions for the centrifugal fan to calculate the operation point mentioned in 2.1.3. (Probst and Pritz (2019))

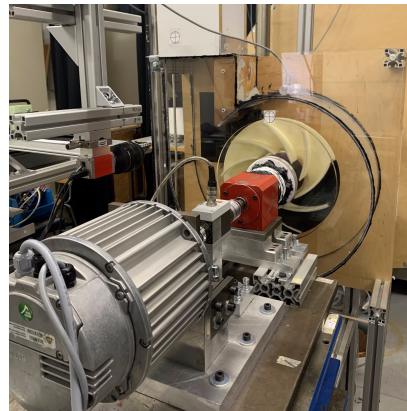


Figure 3.2: Powertrain and centrifugal fan in volute casing.

3.2 2D2C PIV Setup

The utilized facility for this work is set up to run standard 2D2C PIV measurements. In its most basic description, this setup requires a light source, tracer particles and a camera. This section serves to explain the different PIV components used throughout the experiments for this work.

3.2.1 Tracer Particles

Having taken into account the examined considerations in subsection 2.2.1 for the seeding, Di-Ethyl-Hexyl-Sebacat (DEHS) particles were chosen to run the experiments. The use of DEHS

is common for PIV measurements in aerodynamic applications. This is due to the fact that, when atomized in air, DEHS droplets produce a response time of $\approx 2\mu s$ on account of their small diameter ($0.5\text{-}1.5\mu m$) rendering the effects caused by the difference in densities between the droplets and the flow negligible. (Ragni et al. (2011))



Figure 3.3: DEHS tank with atomizer.

3.2.2 Laser and Sensor

In order to maintain the distance between the laser sheet and camera sensor constant when moving across the cross section for the spiral casing, the laser and camera were mounted on a traverse. This assembly is composed of a high intensity, double-pulsed Nd:YAG laser, a charge-coupled device (CCD) sensor and a motorized traverse, pictured in Figure 3.4. Different lenses were considered throughout this work with the goal of varying the captured field of view inside the spiral casing. Ultimately, the experiments were run with a 35mm Nikon lenses. Lenses with larger focal lengths were disregarded due to the small size of their resulting field of view for the spiral casing. In the case of smaller focal lengths the opposite took place. Their resulting fields of view were too wide, therefore reflections from the acrylic glass on the left side of the region of interest (see subsection 3.2.4) were constantly in frame.

Specifications for the sensor used can be seen in table 3.2.

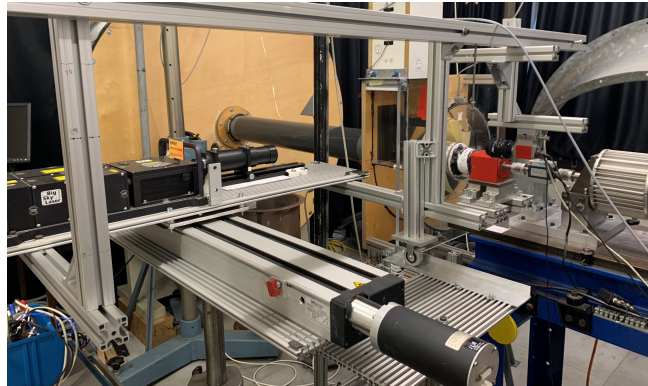


Figure 3.4: Laser/Camera assembly used during the investigation. The laser sitting on the motorized traverse can be seen on the left and the camera attached to the laser and traverse via aluminum bars can be seen on the right.

Property	Value
Resolution (L_x, L_y)	1392 px x 1040 px
Max. frame rate	7.3 / 13.5fps (12 / 24 MHz)
Pixel size ($pixel_{size}$)	6.45 μm x 6.45 μm
Exposure time	1 μs ... 60 s
Dynamic range	A/D 14 bit

Table 3.2: Specifications for the sensor used.

3.2.3 Calibration

With the aim of translating image particle displacements into physical displacements, a calibration for the used lens was required. During previous investigations, a calibration arm was used which consisted of multiple aluminum bars that were anchored outside of the spiral casing and a calibration target which was extruded into the spiral casing. This arm was replaced on the account that it involved a lengthy procedure to assemble and disassemble. Additionally, the distance from the back wall of the spiral casing to the surface of the target was dependent on the position of the anchor point, which was not exact and therefore introduced an unnecessary margin of error during calibration.

This was replaced by a simpler and more accurate calibration plate which was inspired by the original back wall cover for the spiral casing. This plate is extruded to a known distance from the back wall and contains a calibration target along with a reference point with known coordinates from the axis of rotation for the impeller. This allows for any point in the images to be related to the global coordinate system. Both calibration devices can be seen in Figure 3.5.



Figure 3.5: Previous and current calibration devices, respectively.

To convert the image particle displacement from pixels to millimeters, a conversion factor C_f must be extracted. For this, the designed calibration plate was used. The laser sheet was first aligned with the front surface of the calibration plate. This allows the extraction of the z-position for the laser sheet with respect to the global coordinate system for the spiral casing and was achieved by moving the camera/laser assembly with the help of the traverse. Subsequently, the camera was focused on the calibration sheet comprised of a 2×2 mm grid located on the surface of the plate in order to take a proper image of it. This image was called `target.b16` and saved to the correct location in the case folder (see subsection 3.3.2 for the file structure). The camera should at this point be in focus for the particles going through the laser sheet once the experiment is started. Nevertheless, some minor adjustments might be necessary.

Once the calibration image was captured, the pixel distance between the millimeter grid should be measured manually or with the help of a script. This process was performed at different locations and lengths and then averaged in order to obtain a more accurate value. The following general formulas were used:

$$C_{f,i} = \frac{\text{pixel distance}}{\text{millimeter distance}} \quad (3.1)$$

$$C_f = \frac{1}{N} \sum_{i=1}^N C_{f,i}. \quad (3.2)$$

Figure 3.6 shows the calibration image for the used lens with a resulting conversion factor C_f of 13.88 px/mm.

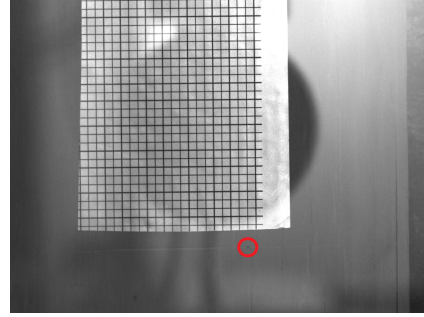


Figure 3.6: Target image for a 35mm lens. Reference point is circled for clarity.

3.2.4 Region of Interest

Multiple configurations exist for the camera/laser assembly in order to measure different regions of interest throughout the spiral casing. Using the traverse allows the capturing of the entire volume for a given area of interest. This area of interest can be varied by changing the position of the sensor with respect to the laser. The choice for it drastically affects the expected flow characteristics since the velocity fields inside the volute casing for a centrifugal fan vary immensely. These variations broaden the factors involved in the determination of optimal parameters for a PIV measurement.

On this account, the extents of this work were limited to a determined area of interest pictured in Figure 3.7. All coordinates were related to the global coordinate system placed at the front end of the axis of rotation for the impeller by means of the reference point mentioned in subsection 3.2.3. The reference point, local and global coordinate systems for the image acquisition setup used can also be found in Figure 3.7.

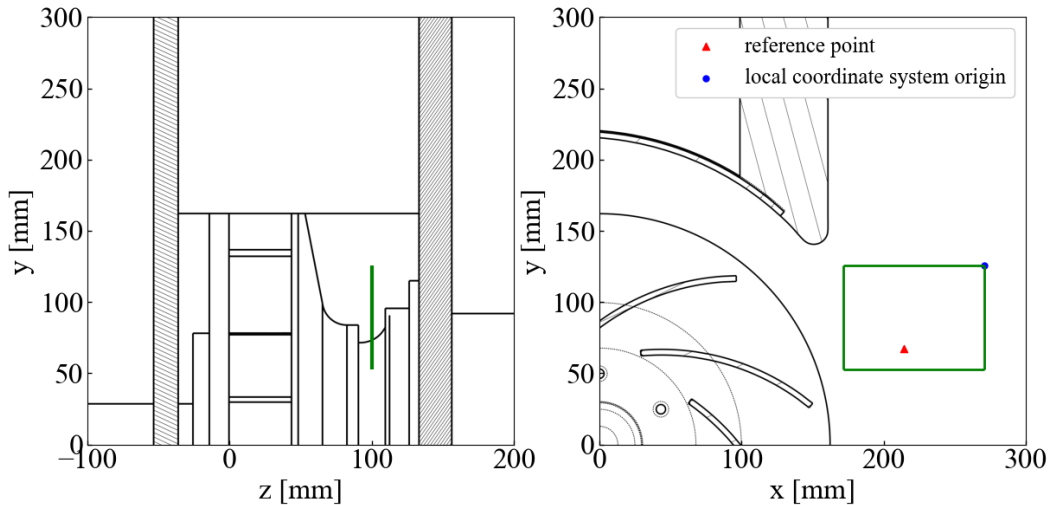


Figure 3.7: Region of interest inside spiral casing. Global coordinate system is described by the figure axes.

3.2.5 Image Acquisition

After a correct calibration for the measurement at hand is performed, the setup should be prepared for the image capturing process. Multiple elements around the investigation area have the ability of becoming a source of unwanted reflections. These reflections are not only bad for the measurement as they contribute to image noise, but could also be harmful for the camera sensor. If the sensor is exposed to high light intensities, it could result damaged. For these reasons, the back wall for the spiral casing was coated with non-reflective black paint and surfaces around the laser sheet were attempted to be kept as smooth and clean as possible. Nevertheless, small scratches in the back wall and acrylic glass are inevitable.

Subsequently, the seeding density, camera/laser synchronization and image focus must be examined. For this, the laser should be run at low intensity at first in order to protect the sensor. The laser intensity and camera aperture are then increased gradually until the desired experiment conditions are reached while checking the sensor's histogram. At this point the camera synchronization as well as the image focus should be inspected. A screen capture is done for the synchronizer settings once the desired conditions are achieved and stored in the plane folder for later reference. Figure 2.9 demonstrates examples of aberrations due to out-of-sync and out-of-focus image samples. In the case of poor seeding density (see subsection 2.2.1), more tracer particles can be introduced into the system at this point.

Once these components are set, the image capturing process can be initiated. Alongside the images for the interrogation area, the operation point and efficiency for the experiment are calculated with the help of the LabView software. This is done by measuring the pressure difference between the inlet and outlet positions for the centrifugal fan and the volume flow through the return pipe (see subsection 2.1.3). In the case of a multi-plane PIV experiment the traverse can be moved by a set interval once the measurements for a plane are complete. This process is then repeated for the remaining planes.

3.3 PIV Evaluation

Following the image acquisition, a PIV measurement is evaluated to extract the velocity fields for a given case. Multiple approaches resulting in varying results can be taken during this procedure, therefore a correct choice of parameters must be done. This section deals with the description of the methods used throughout this work for the image pre-processing and evaluation for a PIV experiment.

3.3.1 Velocity Field Analysis

Unwanted reflections during the image capturing process can lead to high spurious vector counts. For this reason, two techniques were utilized to reduce the effect these reflections have on the image evaluation.

A collection of scripts was developed by *M. Probst* with the goal of accelerating and enhancing the measurement and evaluation processes. Within this collection, a background recognition script was written. This script runs through a set number of images in the measurement and identifies the elements that are part of the background, resulting in two images (`bg_a.tif` and `bg_b.tif`) which are then used when running the PIV evaluation to exclude the background from being analyzed. Furthermore, a mask is used to exclude high reflection zones. The use of both techniques greatly increases the quality for the image evaluation at the expense of a small loss of information. Figure 3.8 shows sample images for the background subtraction and image masking processes.



Figure 3.8: Sample image with undesired reflections (left), background for the image extracted with the background removal script (middle), manually designed mask for high reflection area exclusion (right)

Following the background image extraction and image masking, the desired parameters for the PIV evaluation must be chosen. At this point, the pre-processing, evaluation and outlier detection parameters are chosen. These include image rotation, flipping, filtering, interrogation window dimensions, overlap, correlation algorithm, outlier tests and many others. This process was expedited with the help of python scripts designed to create, distribute and run parameter files with the desired configurations for each investigation. Results are then stored in a single `.hdf` file which allowed easy access to all the pertinent data required for the various plots and analyzes carried out during the investigation. A thorough explanation on the structure for the scripts and data is done in the following subsection.

Due to time constraints and the length for the image pre-processing and outlier detection parameters list (namely filtering), only investigations into the evaluation parameters were carried out during this thesis. Nevertheless, it is worth mentioning that a median filter with outlier interpolation and, in some cases, a minimum to maximum filter were used during the investigations to increase measurement quality.

3.3.2 Data Management

As mentioned in subsection 3.3.1, two python packages were developed by *M. Probst* during the duration of this thesis to aid the measurement and evaluation processes.

The `fan_toolbox` package was written specifically for the facility at hand but it could also be modified for applications in different test benches. It was created with the goal of aiding

the evaluation process and is comprised of multiple scripts dealing with the repeatability and automation of PIV evaluations.

The strudaset package was written with the goal of supporting the handling of data by compressing all the pertinent information regarding a measurement into one single .hdf file. This includes metadata, evaluation results, performance curve measurements and interpreted results. All this information is then easily accessible through the implementation of the data object `Strudaset` in the strudaset package. In this object, the information from the .hdf file is stored as a 5-dimensional array which contains plane (z), time (t), x- and y-coordinates and vector information (v).

4 Methodology and Results

The choice of optimal image acquisition and evaluation parameters for a PIV experiment are investigated in the following chapter. Multiple investigations were carried out regarding both processes and their effects on the measurement quality. It is worth noting that while this investigation was tailored for the setup at hand, the approaches and comparisons are valid for any PIV setup.

4.1 Influence of Interrogation Window Size

For this section, an investigation into the optimal interrogation window dimensions for a PIV measurement based on the flow and setup characteristics was carried out. Multiple components were taken into consideration and are thoroughly explained in each subsection.

4.1.1 Notation, Values and Assumptions

For this work, capitalized variables are used to describe values in the image plane and lower-case variables are used to describe values in the physical plane(X vs x). All variables can be given in millimeters and pixels regardless of which plane is being discussed. The pixel size for a sensor $pixel_{size}$ is used to switch between units in the image plane and the conversion factor C_f is used in the physical plane. In order to relate a measurement between both planes, the magnification M_o is used. Some values were taken as constant and therefore as given.

Parameter	Value
λ	$532 \cdot 10^{-6} \text{ mm}$
L_x	1392 px
L_y	1040 px
$pixel_{size}$	$6.45 \cdot 10^{-3} \text{ mm/px}$
d_p	$1.5 \cdot 10^{-3} \text{ mm}$
$\frac{c_\tau}{d_\tau}$	0.1

With λ being the wavelength for green light, L_x and L_y the sensor resolution, $pixel_{size}$ the sensor pixel size, d_p the average particle diameter, d_τ the recorded particle image diameter and c_τ a system quality constant usually 1 to 10% of d_τ .

The following assumptions were also considered: (Olsen and Adrian (2000))

1. All seeding particles have the same diameter d_p
2. The entire field of view is illuminated with equal laser intensity
3. All particles emit light isotropically
4. All particles emit an equal amount of light
5. Only in-focus particles are illuminated

4.1.2 Optimal Interrogation Window Dimensions

Volume Flow Rate and Exposure Time Delay Dependence

In order to calculate the optimal parameters for the evaluation of a PIV measurement, its average pixel displacement in every direction must be extracted first since every calculation is dependent on these variables. These in turn are a function of the average velocities in vertical and horizontal directions.

Two possible methods exist in order to extract these displacements for a given experiment:

1. **CFD Extraction:** The average velocity components can be extracted from CFD simulations, yielding a rough idea of the pixel displacements in both directions with a known exposure time delay and a given conversion factor. This method, while completely valid, could lead to erroneous choices for the PIV processing since CFD does not account for inaccuracies between the experimental setup and the inputted parameters.
2. **Coarse PIV Run:** A rapid PIV evaluation with a coarse interrogation window (usually a 64×64 interrogation window with a 0% overlap using a multi-pass or multi-grid algorithm) is done in order to extract both mean velocity components. This method is preferred due to the fact that it gives a more accurate pixel displacement since it does not have to deal with inconsistencies between experimental and simulated data.

Once the velocity components are extracted, the average pixel displacements can be calculated regardless of the method of choice.

$$\overline{\Delta x}^{(m)} = \bar{u}\Delta t \quad (4.1)$$

$$\overline{\Delta y}^{(m)} = \bar{v}\Delta t \quad (4.2)$$

$$\overline{\Delta X}^{(px)} = 1000 \cdot \overline{\Delta x}^{(m)} C_f \quad (4.3)$$

$$\overline{\Delta Y}^{(px)} = 1000 \cdot \overline{\Delta y}^{(m)} C_f, \quad (4.4)$$

with \bar{u} and \bar{v} being the X and Y components for the average velocity vector and Δt being the exposure time delay between images in seconds.

According to literature, a PIV measurement should be set up in a way such that the average image pixel displacement should be in the 5-10 pixel range in order to avoid erroneous results due to overly small or large image pixel displacements (Hain and Kähler (2007)). Nevertheless, this range can be extended up to 50 pixels for certain applications (Raffel et al. (2018)). For this reason, an investigation into the optimal pixel displacement for the setup at hand was carried out in section 4.2.

Once a correct time delay is chosen, the following calculations can be done with the extracted average pixel displacements:

$$\overline{\Delta X} = \overline{\Delta X}^{(px)} \cdot pixel_{size} \quad (4.5)$$

$$\overline{\Delta Y} = \overline{\Delta Y}^{(px)} \cdot pixel_{size}, \quad (4.6)$$

Equation 4.6: X and Y particle image displacements in mm.

with the optimal interrogation window dimensions:

$$D_{Ix} = 2 \cdot \overline{\Delta X}^{(px)} \quad (4.7)$$

$$D_{Iy} = 2 \cdot \overline{\Delta Y}^{(px)}, \quad (4.8)$$

rounded to closest integer and doubled to account for the one-quarter rule (see 2.2.2). The validity for these dimensions is investigated in 4.1.3.

Relative Uncertainty, Dynamic Velocity Range and Dynamic Spatial Range

Due to the qualitative nature of PIV, statistical methods have been designed to quantify the quality for a PIV evaluation. For this, the relative uncertainty and dynamic velocity and spatial ranges are calculated for a given measurement with the following procedure.

First, the image line pairs per millimeter lp_m as well as the magnification M_o should be calculated:

$$lp_m = \frac{1}{2 pixel_{size} \sqrt{2}} \left[\frac{1}{mm} \right] \quad (4.9)$$

Equation 4.9: The factor $\sqrt{2}$ in the denominator is defined as such because the sample images are taken as monochromatic. In the case for colored images, this factor is taken as 2.

$$M_o = pixel_{size} \left[\frac{mm}{px} \right] \cdot C_f \left[\frac{px}{mm} \right]. \quad (4.10)$$

Once these values are known, the precision calculation follows. For this, the diffraction limited spot diameter d_s , the optical image diameter d_e and the spatial resolution for the recording system d_r are needed.

$$d_s = 2.44 (1 + M_o) f^\# \lambda \quad [mm] \quad (4.11)$$

$$d_e = \sqrt{d_s^2 + M_o^2 d_p^2} \quad [mm] \quad (4.12)$$

$$d_r = \frac{2}{lp_m} \quad [mm], \quad (4.13)$$

taking $f^\#$ as the lens focal ratio and λ as the wavelength for green light. Consequently, the laser sheet thickness δ_z , recorded image particle diameter d_τ and the system quality constant c_τ can be calculated.

$$\delta_z = 4\left(1 + \frac{1}{M_o}\right)^2 f^{\#2} \lambda \quad [mm] \quad (4.14)$$

$$d_\tau = \sqrt{d_e^2 + d_r^2} \quad [mm] \quad (4.15)$$

$$c_\tau = 0.1 \cdot d_\tau , \quad (4.16)$$

yielding for the measurement precision $\sigma_{\Delta X^{(px)}}$ (Adrian (1997)):

$$\sigma_{\Delta X} = d_\tau c_\tau \quad [mm] \quad (4.17)$$

$$\sigma_{\Delta X^{(px)}} = \frac{\sigma_{\Delta X}}{pixel_size} \quad [px] . \quad (4.18)$$

This is a measure for the ability of estimating the displacement of a particle image ensemble within an interrogation window. The calculation of the quality indicators for an evaluation follows immediately, starting with the relative uncertainty RU :

$$RU_X = \frac{\sigma_{\Delta X}}{\bar{\Delta X}} \quad [\%] \quad (4.19)$$

$$RU_Y = \frac{\sigma_{\Delta Y}}{\bar{\Delta Y}} \quad [\%] \quad (4.20)$$

$$RU = \sqrt{RU_X^2 + RU_Y^2} . \quad (4.21)$$

If the maximum allowable displacement inside an interrogation window c_{max} is taken following the one-quarter rule:

$$\Delta X_{max} = D_{Ix} \cdot pixel_size \quad (4.22)$$

$$\Delta Y_{max} = D_{Iy} \cdot pixel_size \quad (4.23)$$

$$c_{max,X} = \frac{1}{4} \cdot \Delta X_{max} \quad (4.24)$$

$$c_{max,Y} = \frac{1}{4} \cdot \Delta Y_{max} , \quad (4.25)$$

the ratio of maximum to minimum resolvable displacements, or Dynamic Velocity Range (DVR) yields:

$$DVR_X = \frac{c_{max,X} [mm]}{\sigma_{\Delta X} [mm]} = \frac{U_{max,X}}{\sigma_U} \quad (4.26)$$

$$DVR_Y = \frac{c_{max,Y} [mm]}{\sigma_{\Delta X} [mm]} = \frac{U_{max,Y}}{\sigma_U} \quad (4.27)$$

$$DVR = \sqrt{DVR_X^2 + DVR_Y^2}, \quad (4.28)$$

with the maximum and minimum resolvable velocities U_{max} and σ_U respectively:

$$U_{max,X} = \frac{c_{max,X}}{\Delta t} \quad (4.29)$$

$$U_{max,Y} = \frac{c_{max,Y}}{\Delta t} \quad (4.30)$$

$$\sigma_U = \frac{\sigma_{\Delta X}}{\Delta t}. \quad (4.31)$$

For the range of resolvable scales, or Dynamic Spatial Range (DSR):

$$DSR_X = \frac{L_X [px]}{D_{I,X} [px]} \quad (4.32)$$

$$DSR_Y = \frac{L_Y [px]}{D_{I,Y} [px]} \quad (4.33)$$

$$DSR = \sqrt{DSR_X^2 + DSR_Y^2}. \quad (4.34)$$

The DVR and DSR for an evaluation are inversely proportional to each other and have a limit for the total increase between both values $DVR \cdot DSR = const.$. Since they should be maximized, a balance must be established between the two. This limit is calculated with:

$$(DSR \cdot DVR)_X = \frac{L_X [px]}{\sigma_{\Delta X(px)} [px]} \quad (4.35)$$

$$(DSR \cdot DVR)_Y = \frac{L_Y [px]}{\sigma_{\Delta X(px)} [px]}, \quad (4.36)$$

which state the capability of a PIV system to have both a large dynamic velocity range and a large dynamic spatial range in vertical and horizontal directions. These limits are given by the constants $L_X/\sigma_{\Delta X(px)}$ and $L_Y/\sigma_{\Delta X(px)}$ which are characteristic of the system (Adrian (1997)). Knowing this and also that the displacement a particle can have in between two images ΔX and ΔY is a function of the time delay in between exposures Δt , leaves this ratio as a function of only two factors: the time delay between exposures Δt and the volume flow rate \dot{V} (which dictates the interrogation window dimensions). Therefore, a correct balance in between these two variables should be investigated in order to maximize both DVR and DSR values.

4.1.3 Validation

To validate the calculated optimal interrogation window dimensions, a further analysis on the results must be done. For this, multiple interrogation windows are compared to the calculated optimal dimensions. Only interrogation window dimensions that follow the one quarter rule are considered, therefore no dimensions lower than the calculated values are valid.

As mentioned in 4.1.2, the $DVR \cdot DSR$ limit should be maximized, therefore the limit calculated with the optimal dimensions is compared to the limits for other interrogation window dimensions. For this investigation, an optimal interrogation window of 14×24 pixels was considered. This analysis can be done for any calculated dimensions regardless of velocity components. The optimal dimensions will always be the smallest values since only values following the one-quarter rule are considered. All points are normalized by the maximum value.

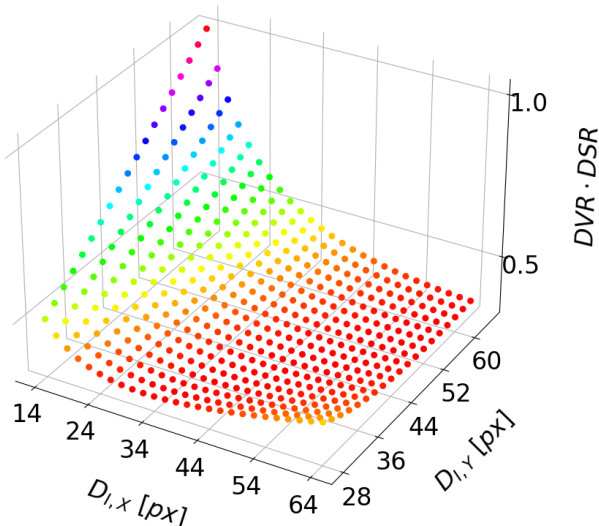


Figure 4.1: $DVR \cdot DSR$ limit for different interrogation window dimensions normalized by the maximum value.

Furthermore, this limit should also have an even distribution between the Dynamic Velocity Range and the Dynamic Spatial Range, therefore the difference between these two values should be minimized. For this, every dimension pair alongside with the ratio between their DVR and DSR values is compared:

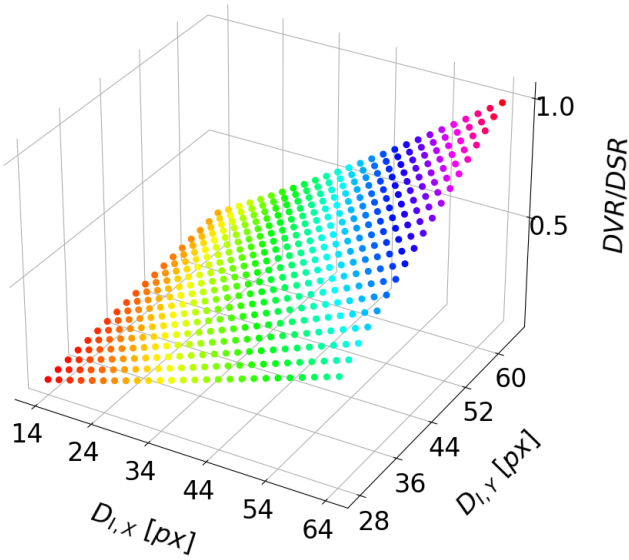


Figure 4.2: Dynamic Velocity Range and Dynamic Spatial Range ratio.

From Figure 4.2, it is evident that the distribution of values inside the limit is more evenly dispersed as the interrogation window dimensions are decreased.

Finally, the ratio between both of these comparisons is investigated. Since the value for the limit should be maximized and the difference between the DVR and DSR minimized, the result for the optimal dimensions should be maximal for:

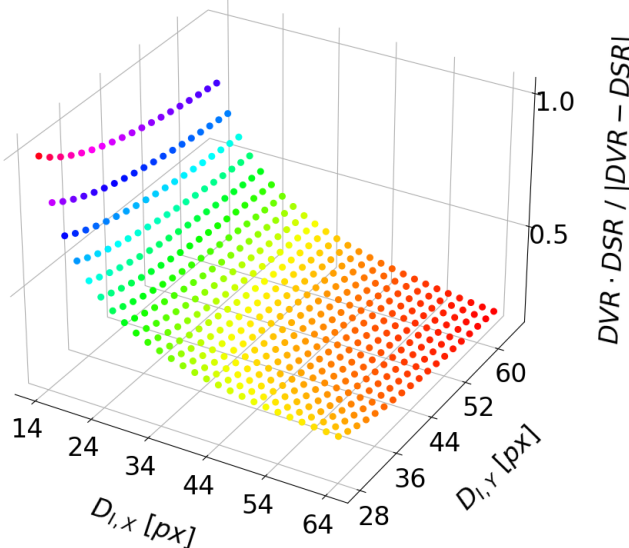


Figure 4.3: Optimal interrogation window dimensions for 14x28 pixels, normalized by the maximum value.

With the comparison in 4.3, it becomes evident that the calculated interrogation window dimen-

sions offer the best limit/distribution value.

4.2 Optimal Particle Image Displacement

As previously stated, the mean particle image pixel displacement is dependent on the measurement operation point and the choice of time delay in between exposures. This dependency does not only affect the magnitude of the pixel displacement, but also the distribution between the vertical and horizontal directions. For this reason, the relationship between the vertical and horizontal pixel displacements was investigated specifically for the experimental setup. This relationship was done by using the following equations:

$$\overline{\Delta X}^{(px)} = 1000 \cdot C_f \cdot \bar{u} \Delta t \quad (4.37)$$

$$\overline{\Delta Y}^{(px)} = 1000 \cdot C_f \cdot \bar{v} \Delta t , \quad (4.38)$$

which, for a given measurement, have matching exposure time delays Δt , yielding:

$$\overline{\Delta Y}^{(px)} = \frac{\bar{v}}{\bar{u}} \cdot \overline{\Delta X}^{(px)} \quad (4.39)$$

with the ratio \bar{v}/\bar{u} being a function of the volume flow rate \dot{V} . This ratio was approximated for different operation points for the setup. The relationship between $\overline{\Delta X}^{(px)}$ and $\overline{\Delta Y}^{(px)}$ for their respective operations points can be seen in figure 4.4.

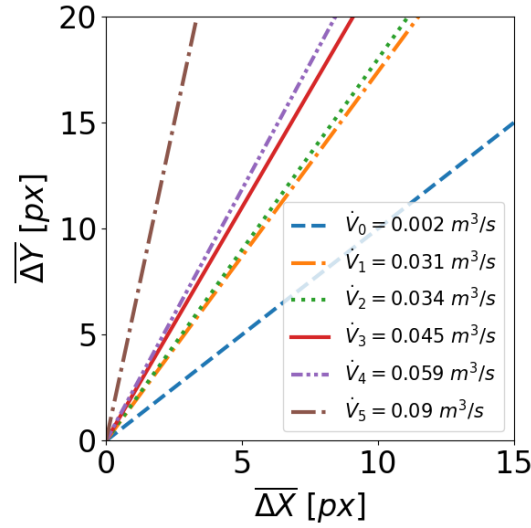


Figure 4.4: Average pixel displacements in vertical and horizontal directions for different volume flow rates. $C_f = 13.88 \text{ px/mm}$.

From Figure 4.4 it can be said that, for the area of interest being investigated, the dominance of the vertical particle displacement increases with the volume flow rate. These relationships

vary for different locations since the flow behavior varies throughout the volute casing (see subsection 3.2.4). Table 4.1 shows the parameters used for each operation point (O.P.) as well as the resulting \bar{v}/\bar{u} ratios.

O.P. #	n_{aux} [rpm]	throttle	\bar{v}/\bar{u}
0	0	0% (closed)	1
1	0	25%	1.74
2	0	50%	1.8
3	0	100% (open)	2.2
4	500	100% (open)	2.37
5	850	100% (open)	5.98

Table 4.1: Operation point parameters. Impeller was attempted to be kept at 600 rpm.

Using these relationships, the quality indicators for varying pixel displacements were calculated, resulting in the following plots.

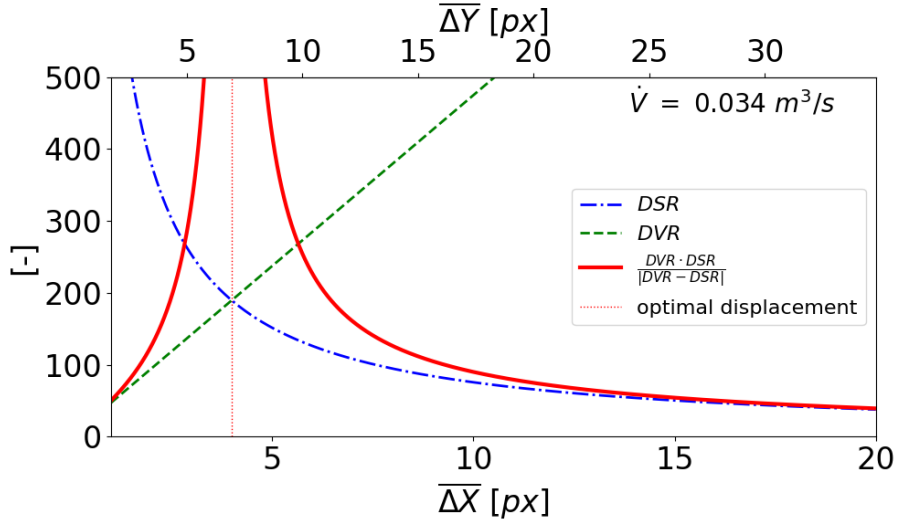


Figure 4.5: Overall quality indicators for a given operation point with varying pixel displacements. Vertical and horizontal displacements resulting in the maximum achievable $DVR \cdot DSR / (DVR - DSR)$ ratio are marked as optimal.

As mentioned in subsection 4.1.2, the DVR and DSR for a given measurement should be maximized while keeping an even distribution between both values. An increasing DSR value translates to a higher spatial resolution. This increase results in a decrease on the DVR of the system, which is not desirable. The optimal particle image displacement in x and y directions resulting in the maximum achievable $DVR \cdot DSR / (DVR - DSR)$ overall value can be extracted from figures similar to Figure 4.5 for all operation points being investigated. This ratio presents the point resulting in the highest possible $DVR \cdot DSR$ limit (see subsection 4.1.2) while keeping the best distribution between both values.

The optimal choice for average pixel displacements can also be visualized by plotting the individual $DVR \cdot DSR / |DVR - DSR|$ ratios in vertical and horizontal directions alongside the overall ratio as seen in figure 4.6.

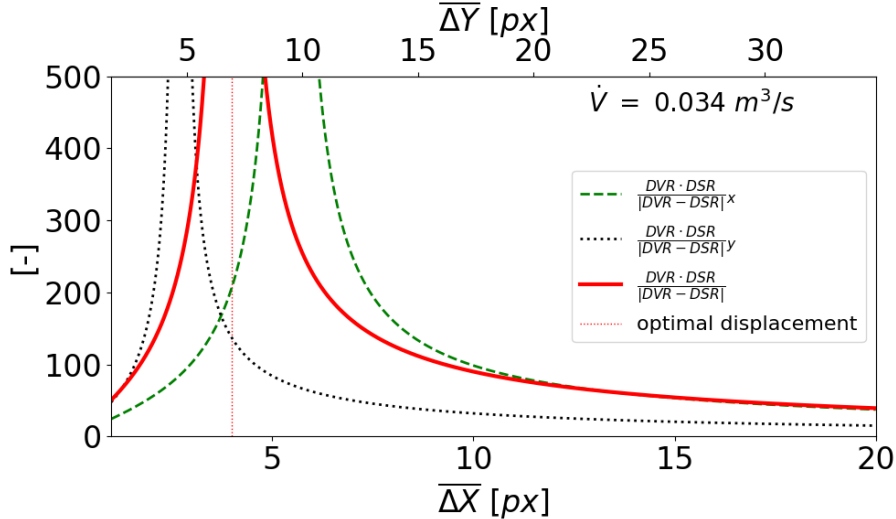


Figure 4.6: Individual quality indicators for a given operation point with varying pixel displacements. Vertical and horizontal displacements resulting in the maximum achievable $DVR \cdot DSR / |DVR - DSR|$ ratio are marked as optimal.

This process was repeated for each operation point being investigated yielding the following values¹:

O.P. #	$\dot{V} [m^3/s]$	$\overline{\Delta X}_{opt} [px]$	$\overline{\Delta Y}_{opt} [px]$
0	0.002	5	6
1	0.031	4	7
2	0.034	4	7
3	0.045	4	7
4	0.059	4	9
5	0.090	3	14

Table 4.2: Optimal average pixel displacements for investigated operation points.

Finally, these values were used to calculate the exposure time delay required to achieve the optimal average particle image displacements Δt_{opt} . Since a relationship between the vertical and horizontal pixel displacements exists, the optimal exposure time delay was only calculated by means of the particle image displacement in y direction.

For this, an ideal, completely vertical flow was first assumed. With this assumption, the exposure time delay Δt was formulated as a function for a given conversion factor C_f , target particle image displacement $\overline{\Delta X}_{opt}$ and the volume flow rate \dot{V} . This function is given by:

¹Figures for the remaining operation points can be found in A.1

$$\Delta t = \frac{1}{1000 \cdot C_f} \cdot \frac{A_{out}}{\dot{V}} \cdot \overline{\Delta Y}_{opt} . \quad (4.40)$$

Figure 4.7 shows the calculated exposure time delays required to achieve the desired particle displacement for a given conversion factor. Experimental results are scattered alongside with an extrapolation to the actual desired particle displacement for the investigated operation points using:

$$\Delta t_{opt,i} = \frac{1}{1000 \cdot C_f} \cdot \frac{1}{\bar{v}_i} \cdot \overline{\Delta Y}_{opt} . \quad (4.41)$$

A best fitting curve through the extrapolated values is plotted as well. The divergence between experimental and calculated results (more clearly seen for smaller volume flow rates) is a result from the complete vertical flow assumption. As a result, this assumption can only be taken for large volume flow rates.

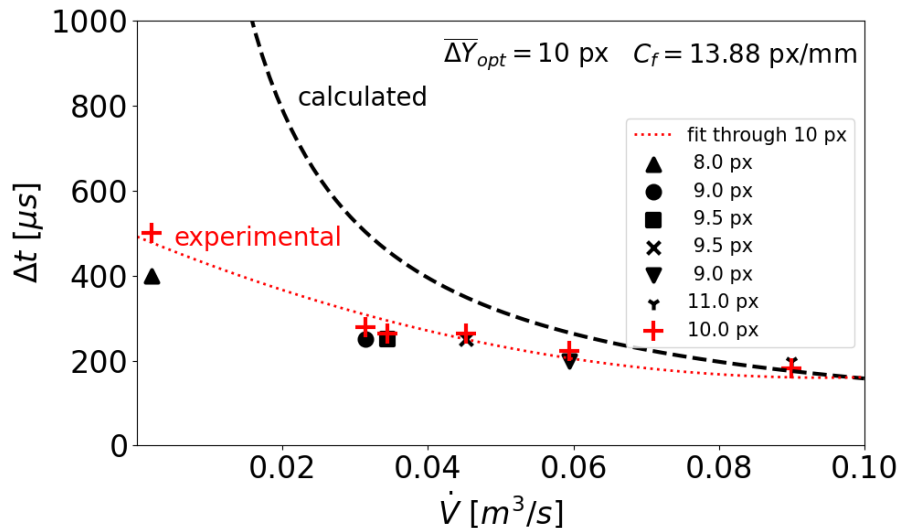


Figure 4.7: Required exposure time delay for a given target particle image displacement with respect to volume flow rate. Calculated values are plotted alongside experimental results with errors (black scatters). Extrapolated values for the target particle image displacement based on experimental results are plotted as well with a best fitting curve (red crosses and dotted line).

4.3 Optimal Interrogation Window Overlap

After the investigation into the optimal interrogation window dimensions is complete, it is worth to investigate further into the optimal choice for its overlap. For this, multiple PIV evaluations were run on a sample experiment. Evaluations were run with a fixed $D_{I,x}$ dimension and varying $D_{I,y}$ dimensions (and vice versa), as well as the overlap percentage. This was done to compare the effect the overlap has on the overall PIV results. A multi-pass algorithm was used with 3 passes over 250 image pairs for each evaluation. All values are averaged over the number of image samples.

First, the number of active vectors for different overlap percentages were investigated. Evaluations with 2 times the interrogation window dimensions and a 50% overlap as well as evaluations with 4/3 times the interrogation window dimensions and a 25% overlap were compared.²

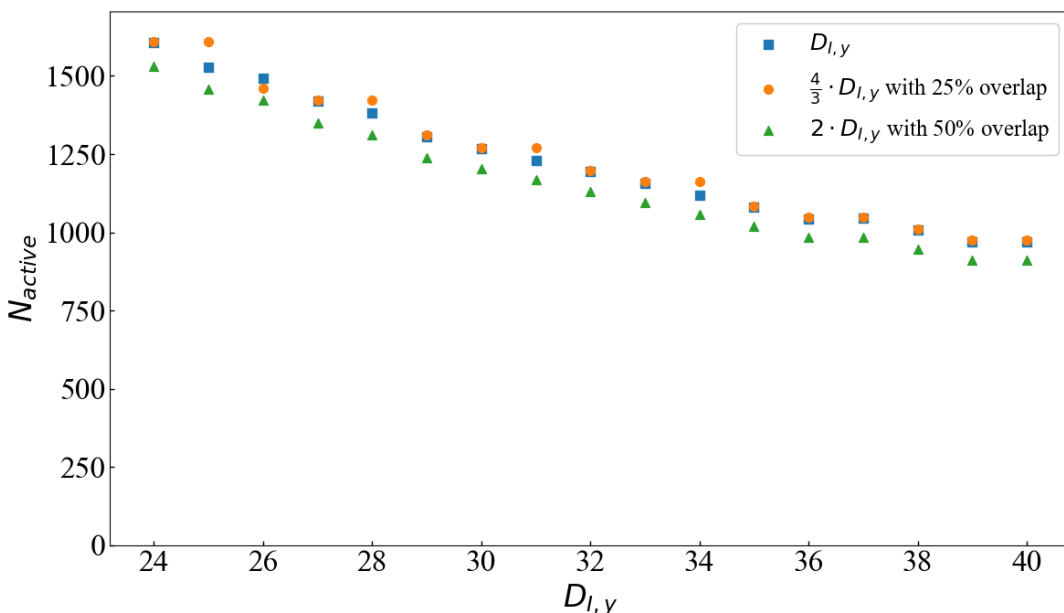


Figure 4.8: Active vectors for PIV evaluations using a multi-pass algorithm.

Generally, the highest possible active vector count for an evaluation is desired. This is because its spatial resolution is directly proportional to this vector count. Nevertheless, the active vector count should as well be as small as necessary given the fact that the number of spurious vectors increases with the active vector count. Therefore, a compromise must be done between these. Figure 4.8 shows that the active vector count for a two times larger interrogation window with a 50% overlap and for a 4/3 times larger interrogation window with a 25% overlap are equivalent to that of a measurement with 0% overlap. This is due to the increase in sampling caused by the overlap percentage (see subsection 2.2.2).

²Overlap percentages larger than 50% are not recommended. (Stamhuis (2006))

From the comparison in Figure 4.8, it becomes evident that the active vector count for a PIV measurement is dependent on the chosen overlap percentage with respect to a given interrogation window dimension. When comparing the active vector count with the valid vector count, it shows how for each overlap variation the active vector count is the same but there is a divergence for the valid vectors. This higher valid vector count seen in Figure 4.9 for a two times larger interrogation window with a 50% overlap translates into a higher quality compared to a measurement with 0% overlap.

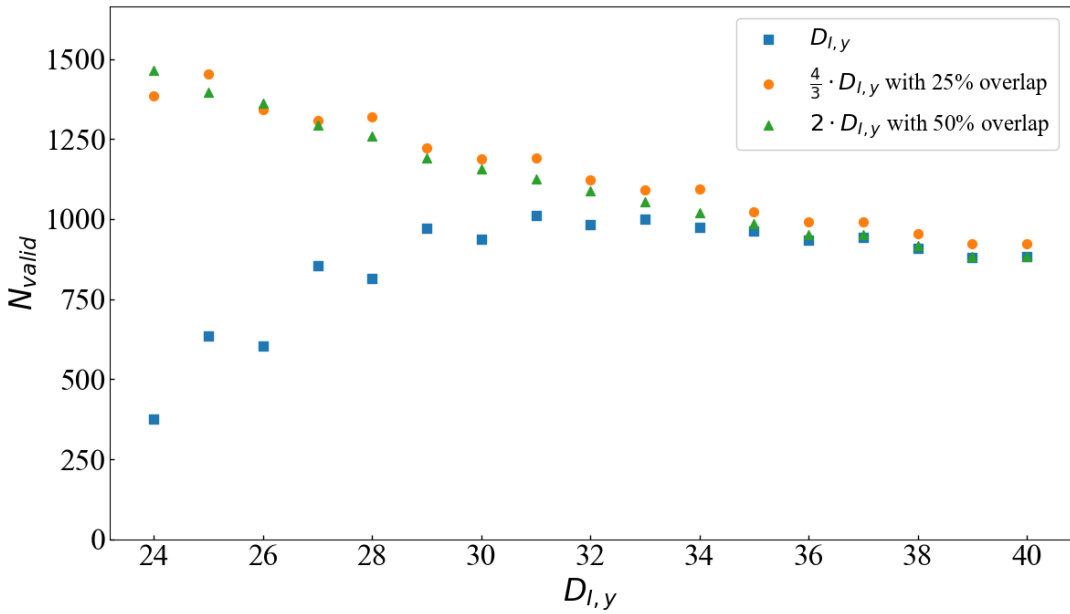


Figure 4.9: Valid vectors for PIV evaluations using a multi-pass algorithm.

Both of these comparisons can be summarized by comparing all three variations' Valid Detection Probabilities (VDPs) seen in Figure 4.10.

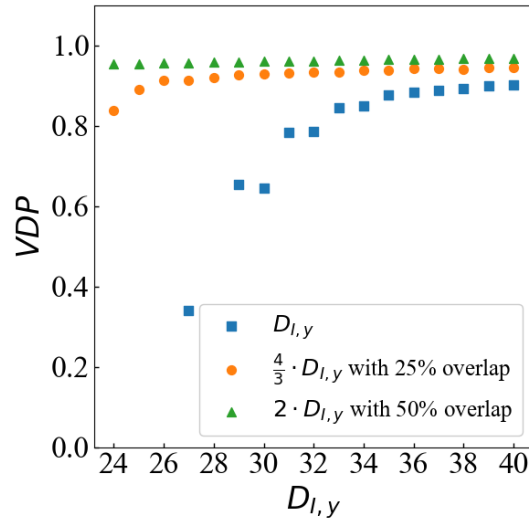


Figure 4.10: Valid detection probability for PIV evaluations using a multi-pass algorithm.

As mentioned in subsection 2.2.3, the VDP for an evaluation is a measure of the valid vector density with respect to the total number of vectors. A VDP value between 90-95% is generally desired in order for the evaluation resolution to be considered appropriate (Raffel et al. (2018)). Figure 4.10 illustrates how the VDP converges inside the desired range for different dimensions when using different overlap percentages. Additionally, a comparison for these evaluations' interpolated and replaced vector counts was done.

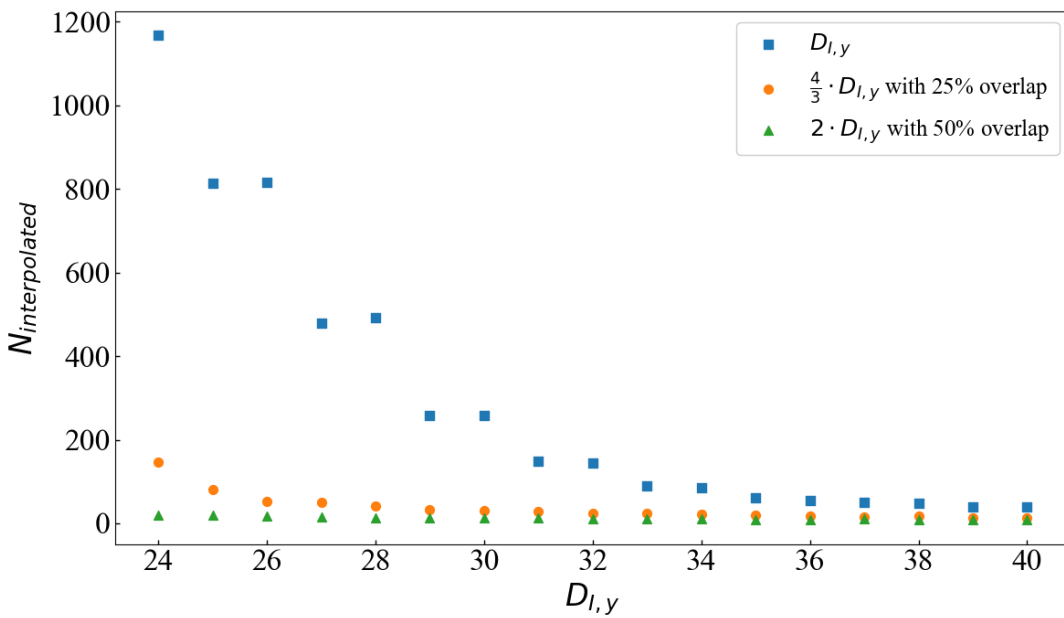


Figure 4.11: Interpolated vectors for PIV evaluations using a multi-pass algorithm.

A decrease for the interpolated vector count can be seen as the overlap percentage is increased in Figure 4.11. This results in a more favorable outcome for the PIV evaluations since the number

of interpolated vectors should be minimized. This same behavior can also be observed when looking at the number of replaced vectors with other correlation peaks:

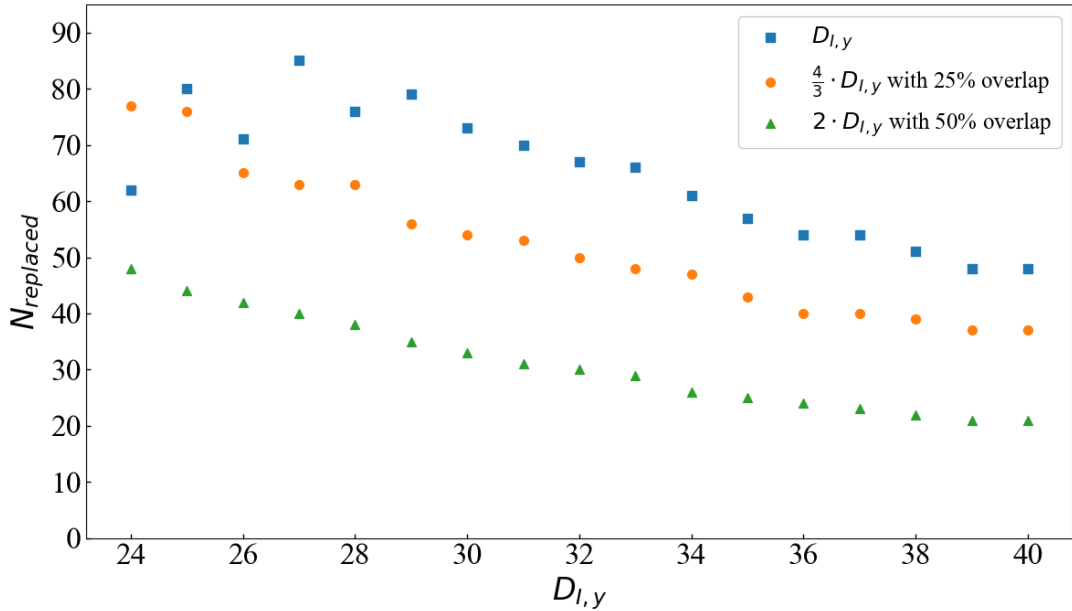
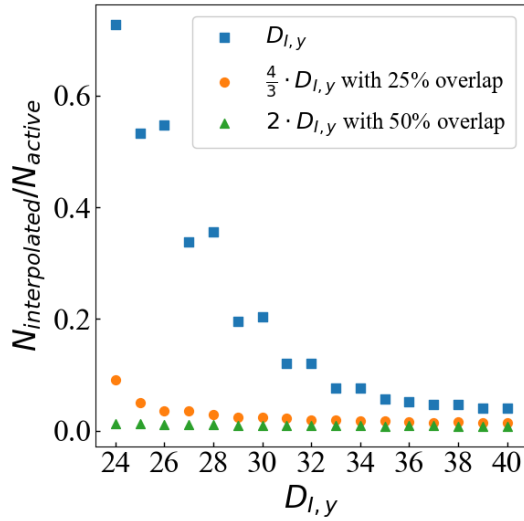


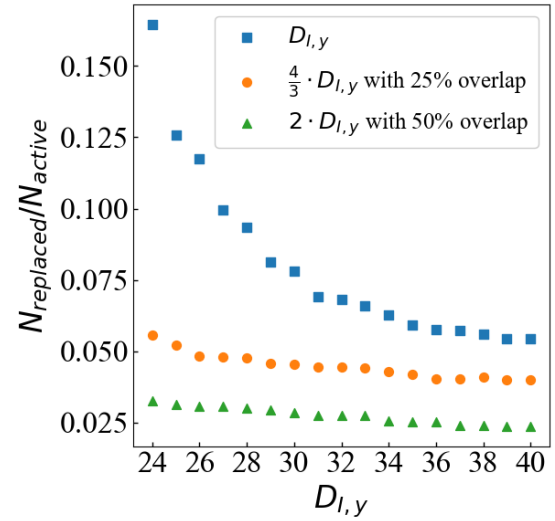
Figure 4.12: Replaced vectors for PIV evaluations using a multi-pass algorithm.

Which is a factor that should be minimized as well.

When comparing the number of interpolated and replaced vectors with respect to the number of active vectors for a 0, 25 and 50% overlap it gives:

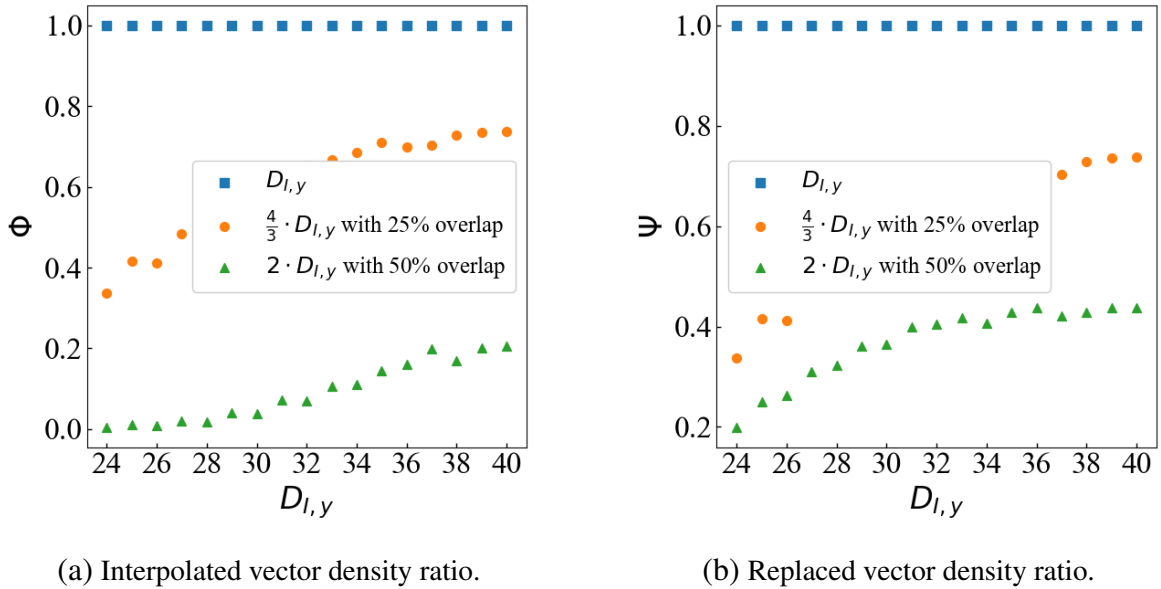


(a) Interpolated vector density.



(b) Replaced vector density.

Further highlighting the interpolated and replaced vector count decrease when a higher overlap is used. This decrease is better visualized if the ratio between the number of flagged vectors per active vectors is compared among the three overlap percentages.



using:

$$\Phi_i = \frac{N_{interpolated,i}/N_{active,i}}{N_{interpolated,0}/N_{active,0}} \quad (4.42)$$

$$\Psi_i = \frac{N_{replaced,i}/N_{active,i}}{N_{replaced,0}/N_{active,0}} \quad . \quad (4.43)$$

Dimension Ratio	Overlap	$\bar{\Phi}$	$\bar{\Psi}$
$D_{I,y}$	0	1	1
$\frac{4}{3} \cdot D_{I,y}$	0.25	0.18	0.60
$2 \cdot D_{I,y}$	0.5	0.09	0.37

Table 4.3: Average interpolated and replaced vector density ratios with respect to results using a 0% overlap.

Table 4.3 shows the average interpolated and replaced vector density ratios with respect to an evaluation with 0% overlap. This means that, on average, using an interrogation window with twice the dimensions and a 50% overlap results in the same amount of active vectors with a 91% decrease in interpolated vector density and a 63% decrease in replaced vector density. It becomes evident that a higher overlap percentage results in a reduction of flagged vector density. This correlates with the results from multiple investigations into the overlap for PIV evaluations. (Hart (2000), Meinhart et al. (1999), Stamhuis (2006))

4.4 Optimal Cross-correlation Algorithm

In this section, three different processing algorithms were compared. The procedure followed in subsection 4.3 was repeated for the single pass, multi-pass and multi-grid algorithms. Evaluations were run over 250 image pairs with a constant $D_{I,x}$ dimension and varying $D_{I,y}$ dimensions with the goal of determining the point of convergence for the individual results.

Previously, it was concluded that a higher overlap percentage yields the best results for a given algorithm, therefore only evaluations using a 50% overlap were considered. The dimensions used for this investigation describe the final interrogation window size in the case of the multi-grid algorithm.

First, the valid vectors for all algorithms were compared by means of their valid detection probabilities (VDP).

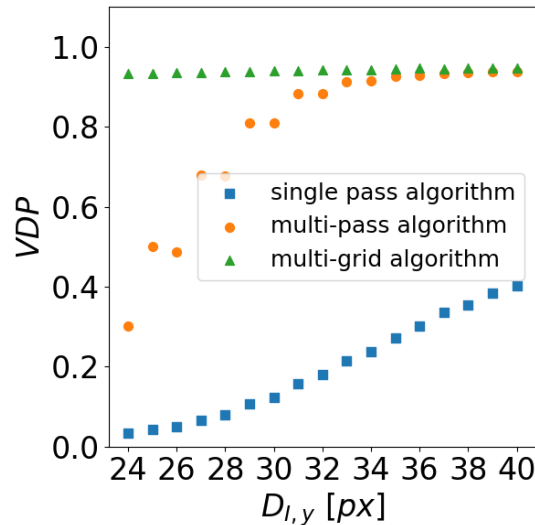


Figure 4.15: Valid detection probability for PIV evaluations.

Figure 4.15 illustrates how the VDP converges inside the desired range of 90-95% for different dimensions when using the multi-pass and multi-grid algorithms while the single pass algorithm remains undesirable for all investigated dimensions. At this point, it is evident that using a multi-grid algorithm allows the use of a higher spatial resolution for an evaluation in the desirable VDP range. In the case for the single and multi-pass algorithms, this spatial resolution must be lower for the evaluation to be in the same range.

Afterwards, the flagged vector densities were compared over the same range of interrogation window dimensions for all algorithms. These include replaced vectors with other correlation peaks and interpolated vectors.

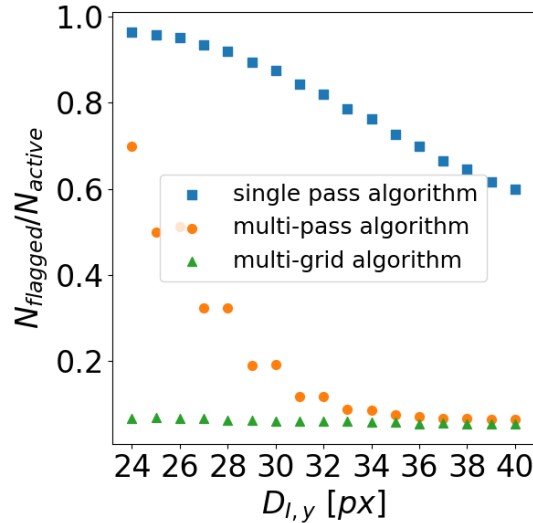


Figure 4.16: Flagged vector count ratio.

As mentioned in section 4.3, flagged vectors should be minimized for a PIV evaluation. A clear contrast can be observed between all three algorithms in Figure 4.16, specially for the single pass. Since both the multi-pass and multi-grid algorithms perform multiple iterations of the evaluation on each double image, they are able to more accurately track the particle movements, resulting in a considerable decrease in vector replacement and interpolation. A reduction in flagged vectors, although smaller than for the single pass, can also be noticed between the multi-pass and multi-grid algorithms.

This reduction is further visualized when comparing the flagged vector densities with respect to the single pass algorithm, seen in Figure 4.17.

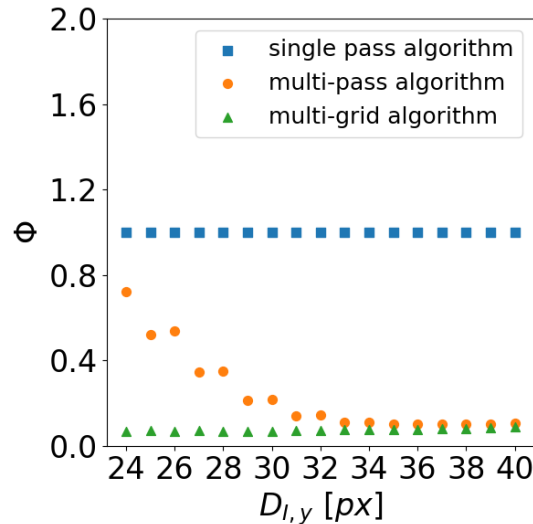


Figure 4.17: Flagged vector density ratio.

using:

$$\Phi_i = \frac{N_{flagged,i}/N_{active,i}}{N_{flagged,singlepass}/N_{active,singlepass}} , \quad (4.44)$$

it becomes evident that using the multi-pass and multi-grid algorithms result in far better measurements when compared to the single pass algorithm. The average flagged density ratios for the multi-pass and multi-grid algorithms with respect to the single pass algorithm can be seen in table 4.4. Here, it can be concluded that using the multi-grid algorithm results in a 92% decrease in flagged vector density on average when compared to the single pass algorithm. In the case for the multi-pass algorithm, the resulting flagged vector density reduction is of 76% on average.

Algorithm	Overlap	$\bar{\Phi}$
Single pass	0.5	1
Multi-pass	0.5	0.24
Multi-grid	0.5	0.08

Table 4.4: Average flagged vector density ratios with respect to the single pass algorithm.

4.5 Optimal Parameters

Following the results from the previous sections, an optimal set of parameters was chosen for given operation points. As mentioned in section 4.2, the optimal particle image displacement is dependent on the volume flow being investigated, therefore making the exposure time delay and interrogation window dimensions dependent on the volume flow rate as well. Table 4.5 shows the optimal acquisition parameters for the investigated operation points.

O.P. #	$\dot{V} [m^3/s]$	$\Delta X_{opt} [px]$	$\Delta Y_{opt} [px]$	$\Delta t_{opt} [\mu s]$
0	0.002	5	6	350
1	0.031	4	7	200
2	0.034	4	7	200
3	0.045	4	7	200
4	0.059	4	9	200
5	0.090	3	14	250

Table 4.5: Optimal acquisition parameters for multiple operation points, rounded to the closest integer.

From sections 4.3 and 4.4, it was concluded that using a multi-grid cross-correlation algorithm with a 50% overlap yields the best results. Therefore, the used optimal evaluations parameters read:

O.P. #	$\dot{V} [m^3/s]$	$D_{I,X} [px]$	$D_{I,Y} [px]$
0	0.002	25	24
1	0.031	16	28
2	0.034	16	28
3	0.045	16	28
4	0.059	16	36
5	0.090	12	56

Table 4.6: Optimal interrogation window dimensions for a multi-grid algorithm using a 50% overlap. Dimensions are doubled due to the use of a 50% overlap.

Previous investigations using PIV as an evaluation technique on this test bench, as well as throughout the investigated literature (Raffel et al. (2018)), utilize a multitude of squared interrogation window dimensions. These are most commonly in the sequence of 16^2 , 32^2 , 64^2 , 128^2 , etc. pixels, depending on the flow characteristics being investigated. In order to compare the calculated optimal parameters to a standard run, a 64×64 interrogation window was used for an additional evaluation using the multi-grid algorithm with a 50% overlap. Using these dimensions guarantees that no additional spurious vectors arise due to oversampling since they are larger than all dimensions from the optimal runs. Additionally, this allows for the difference between the dimensions for both evaluations to be kept relatively small.

Assessments were done by comparing the evaluations' quality indicators over 1500 images. This method allows the visualization for not only the average results, but also for the variance across the images. Compared values include the displacement scatter plots, valid detection probabilities, velocity distribution histograms, dynamic spatial and velocity ranges, limit and distribution, flagged vector densities and finally, the resulting contour and quiver plots. The aforementioned comparisons are only shown for a given operation point ($\dot{V}_2 = 0.0344 \text{ m}^3/\text{s}$). Nevertheless, the average results for all operation points can be seen in Table 4.8 and the plots can be found in A.2.

To begin, the evaluations' dynamic velocity and spatial ranges are compared alongside their distribution ratios.

Evaluation	DVR	DSR	DVR/DSR	$\frac{DVR \cdot DSR}{ DVR - DSR }$
multigrid_16x28_50	381.4	189.2	2.02	375.4
multigrid_64x64_50	1070.5	54.3	19.6	57.2

Table 4.7: Dynamic velocity and spatial range values and ratios for optimal and standard evaluations.

From Table 4.7, a large difference for the spatial and velocity ranges can be seen between both evaluations. In the case of the standard evaluation, a large velocity range is visible. This means that, for that set of parameters, the maximum resolvable velocities are much greater than for the case of the optimal parameters. Nevertheless, these large resolvable velocities might not be needed since this test bench deals with velocities in the 0-6 m/s range.

Conversely, the dynamic spatial range for the standard case is less than one third of the resulting spatial range for the optimal case. This translates to a more than three times lower resolution for the results, which can be visualized by comparing the histograms of the velocity components for both evaluations, seen in Figure 4.18. An almost ten fold increase in vectors can be seen for the case of the optimal evaluation since the vector count and spatial resolution are related to the second degree (see Figure 4.5). From Figure 4.18, it can also be noted that for the optimal evaluation, the measured velocity fluctuations are reduced drastically. This is also desirable since it translates to a more accurate measurement.

As explained in subsection 4.1.2, the parameters for a PIV evaluation must be chosen in a way such that both the DVR and DSR are maximized while maintaining an even distribution among both values. This ensures an optimal resolvable range to information density relationship and can be quantified by the distribution ratio $DVR \cdot DSR / |DVR - DSR|$, which, for this comparison, shows a more than six times larger value for the optimal evaluation.

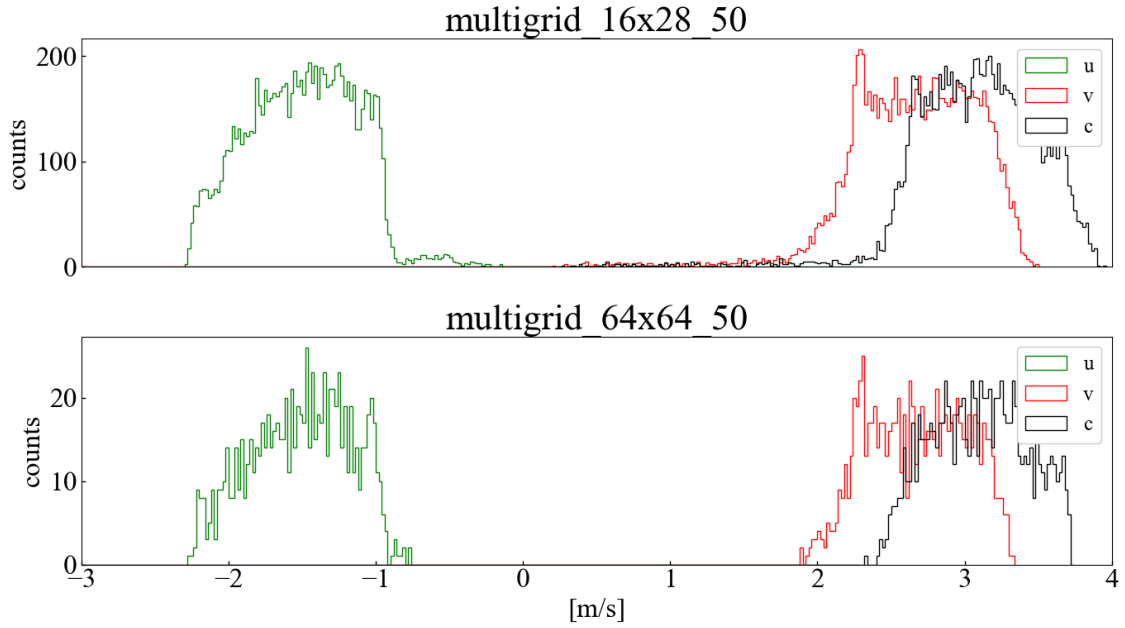


Figure 4.18: Histogram for velocity components for optimal (top) and standard (bottom) evaluations.

As mentioned in subsection 2.2.2, a choice of smaller interrogation window dimensions increases the spatial range for a measurement generally at the expense of its accuracy. For this reason, the valid detection probabilities over all images for both evaluations were compared.

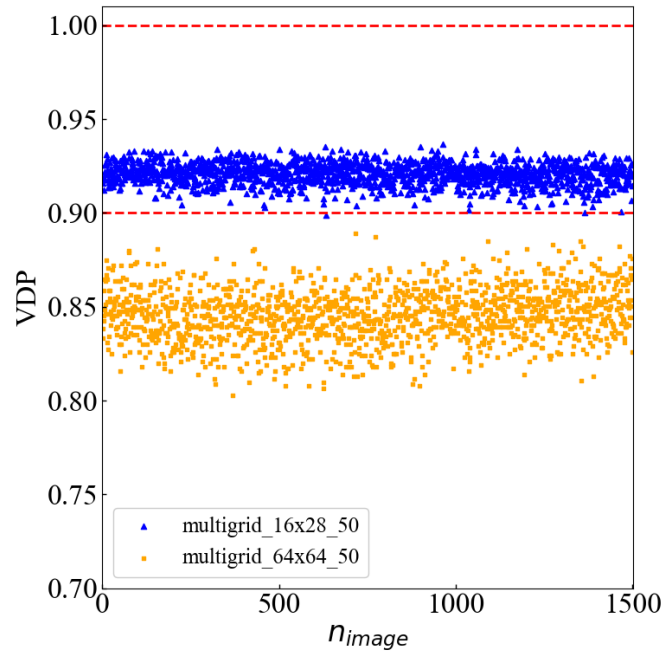


Figure 4.19: Valid detection probabilities (VDP) for optimal and standard evaluations.

The VDP for a measurement quantifies the ratio between its valid and total vector counts. For a measurement to be considered appropriate, this value should be in the range of 90-95%. From Figure 4.19 it becomes evident that, for this case, increasing the spatial range for the optimal evaluation resulted in an increase for its valid vector density. The average VDP over all images for the optimal evaluation results in 92.1% while for the case for the standard evaluation it is 84.6%, well under the desirable region.

Furthermore, the displacement scatter plots and relative uncertainties for both runs were compared. Multiple observations can be made from this comparison. First, the PDFs show the deviation between the average vertical and horizontal velocities for the individual images (\bar{v} and \bar{u} , respectively) and the average vertical and horizontal velocities over all images ($\langle v \rangle$ and $\langle u \rangle$, respectively). This comparison shows that the variations across all images for both evaluations were relatively similar and constant, which is desirable. The same conclusion can be made for the relative uncertainties, which is a measure of the accuracy a PIV evaluation has.

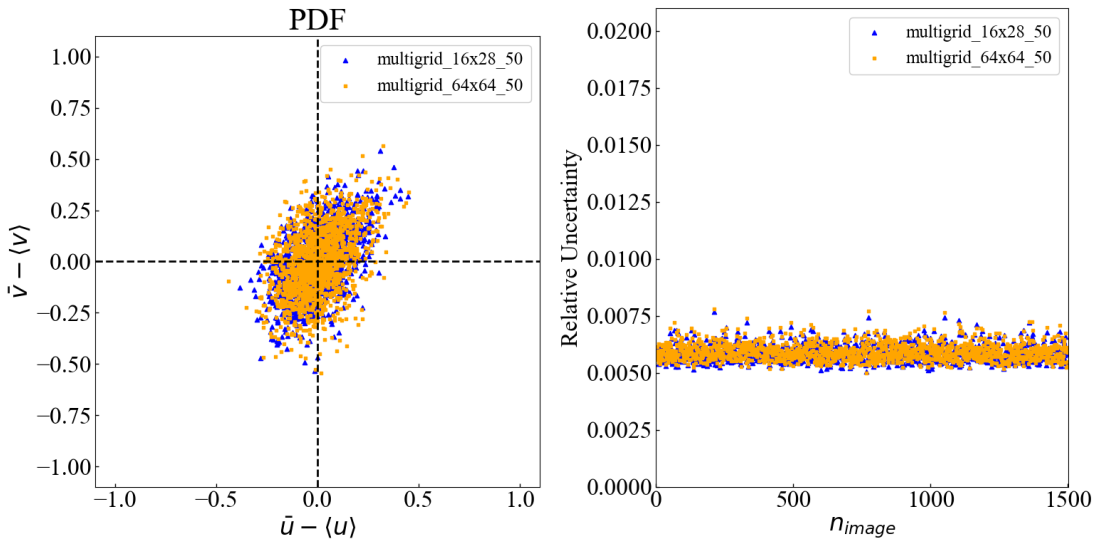


Figure 4.20: Displacement scatter plots (left) and relative uncertainties (right) for optimal and standard evaluations.

The comparisons pictured in Figure 4.20 show that, despite the fact that the spatial resolution was increased for the optimal evaluation which generally would cause an increase in uncertainty, the variations across all images were kept constant when compared to the standard evaluation. This owes to the fact that a careful calculation was done to find the limit at which the spatial resolution could be increased without compromising the quality for the evaluation.

To finalize the comparison, contour plots for both evaluations were assessed. Figure 4.21 shows contour plots for the velocity magnitudes \vec{c} in the area of interest inside the spiral casing for both evaluations. Figure 4.22 shows the same contour plots, enlarged for better detailing. Coordinates are plotted with respect to the global coordinate system located at the axis of rotation for the impeller.

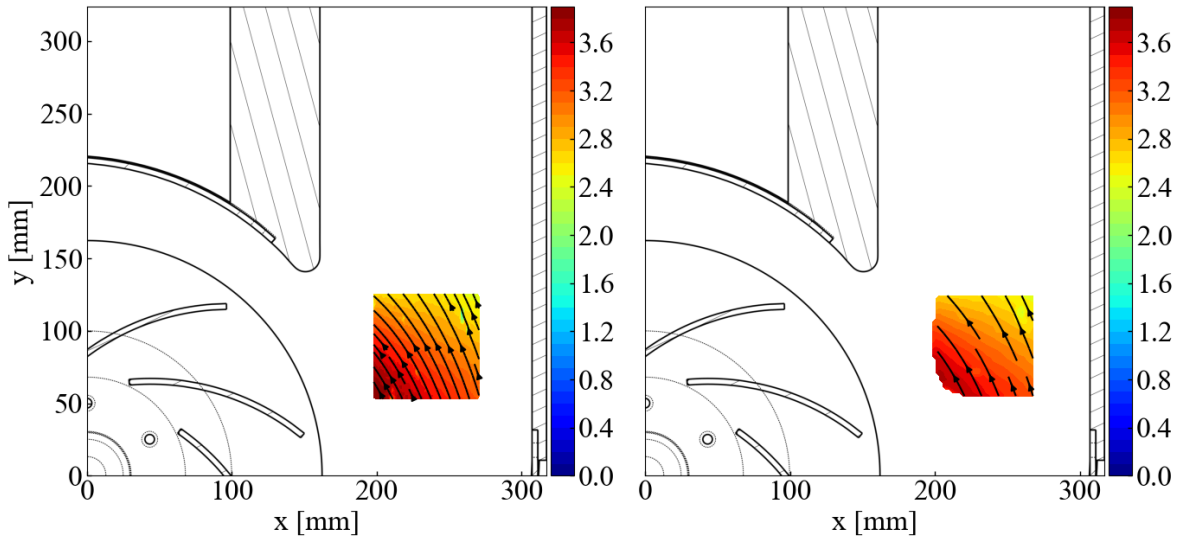


Figure 4.21: Contour plots for the absolute velocities in m/s inside the area of interest in the spiral casing for the optimal evaluation (left) and standard evaluation (right).

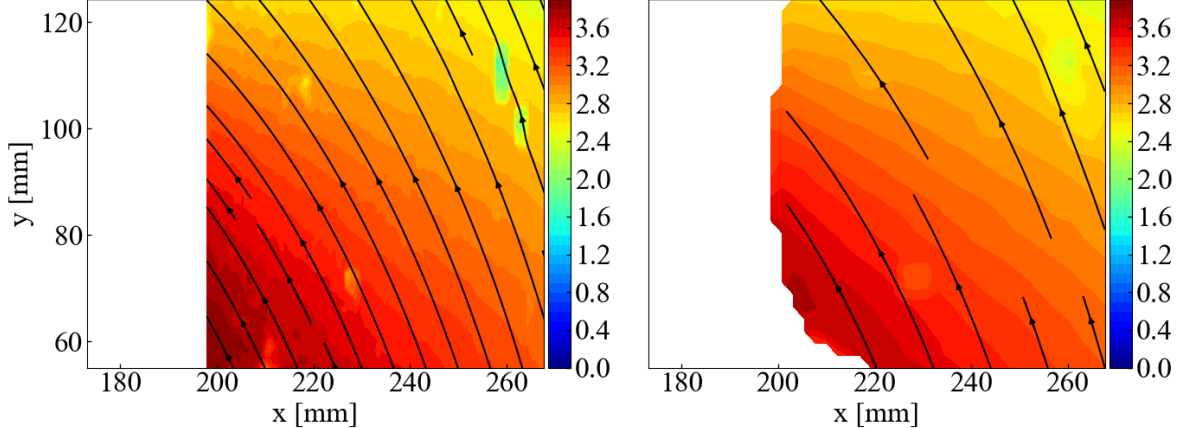


Figure 4.22: Contour plots for the absolute velocities in m/s for the optimal evaluation (left) and standard evaluation (right). White spaces represent masked areas.

From these figures, a clear differentiation can be made. The higher velocity range for the standard parameters resulted unnecessary since all velocities were resolvable for both evaluations. Furthermore, the higher spatial resolution for the optimal evaluation translated in a greater detail for its contour plot. This is noticeable specially in the areas of high velocity fluctuations near the volute tongue for the spiral casing. Additionally, the interpolation for the masked areas on the top right area are clearly distinguished for the optimal evaluation while for the standard they could be interpreted as fluctuations.

For matters of completeness, this comparison was carried out for the remaining investigated operation points, yielding similar results. All averaged results can be seen in Table 4.8 and the plots can be found in A.2.

O.P. #	\dot{V} [m^3/s]	Evaluation	DVR	DSR	DVR/DSR	$\frac{DVR-DSR}{ DVR-DSR }$	VDP	RU
0	0.002	25x24 50%	418.5	137.8	3.03	205.3	0.97	0.005
		64x64 50%	1070.5	54.3	19.7	57.2	0.91	0.005
1	0.031	16x28 50%	381.4	189.2	2.01	375.4	0.91	0.006
		64x64 50%	1070.5	54.3	19.7	57.2	0.82	0.006
2	0.034	16x28 50%	381.4	189.2	2.02	375.4	0.92	0.005
		64x64 50%	1070.5	54.3	19.7	57.2	0.84	0.005
3	0.045	16x28 50%	381.4	189.2	2.02	375.4	0.91	0.006
		64x64 50%	1070.5	54.3	19.7	57.2	0.81	0.006
4	0.059	16x36 50%	466.0	183.3	2.54	302.3	0.92	0.007
		64x64 50%	1070.5	54.3	19.7	57.2	0.73	0.007
5	0.090	12x56 50%	677.4	235.0	2.88	359.7	0.83	0.008
		64x64 50%	1070.5	54.3	19.7	57.2	0.75	0.009

Table 4.8: Final comparisons for optimal and standard evaluations for all investigated operation points.

From Table 4.8 it becomes evident that a significant increase in measurement quality is present when comparing the optimal and standard evaluations for all operation points. On average, the VDPs for the evaluations experienced a 13% increase when using the optimal parameters. Additionally, the evaluation spatial resolution experienced a 245% increase on average over all operation points.

Based on these results, it can be confidently said that the parameters extracted from the carried out investigations produce evaluations that fall in the optimal range for operation points 1 through 4. Consequently, the cases for operation points 0 and 5 require a deeper inspection due to their results falling outside of opposite limits for the desirable VDP range. This problem carries different interpretations for both O.P.'s.

For the case of O.P. 0, the VDP exceeds the optimal range, meaning that the possibility for a greater increase in spatial resolution is available, therefore, an even smaller interrogation size can be used while maintaining an overall desirable evaluation quality. As a result, an additional evaluation was conducted for this measurement using half the interrogation window dimensions.

On the other hand, O.P. 5 experienced the opposite case. An increase in VDP took place when comparing the optimal and standard runs but it still remained in the sub-optimal range. For this, an additional evaluation with dimensions based on the maximum pixel displacement in both directions instead of the mean was done. Resulting values for both additional evaluations

can be seen in Table 4.9 and their resulting VDPs compared to the previous calculated optimal solution are shown in Figure 4.23.

O.P. #	$\dot{V} [m^3/s]$	Evaluation	DVR	DSR	DVR/DSR	$\frac{DVR \cdot DSR}{ DVR - DSR }$	VDP	RU
0	0.002	13x12 50%	218.1	263.8	0.83	1258.9	0.92	0.005
5	0.090	32x80 50%	1019.1	90.8	11.2	99.7	0.90	0.008

Table 4.9: Additional evaluation results for O.P.'s 0 and 5.

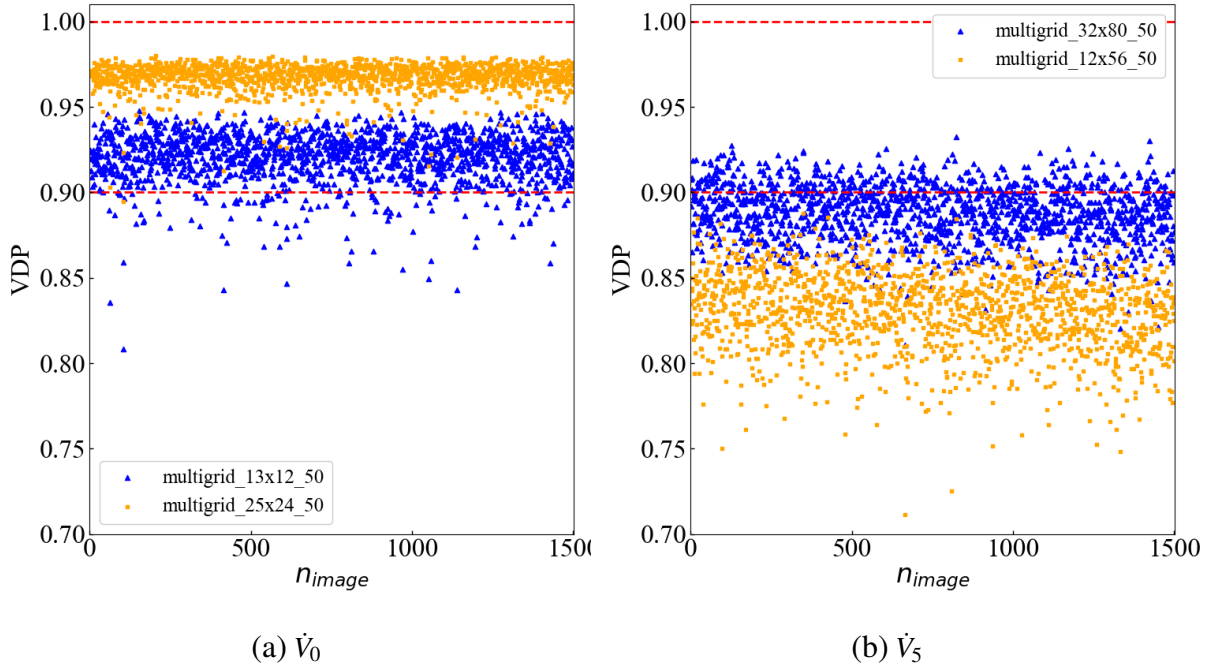


Figure 4.23: Valid detection probabilities (VDP) for additional (blue triangles) and calculated optimal (orange squares) evaluations.

From the results in Table 4.9 and Figure 4.23, it can clearly be seen that the additional evaluations produced better results than the calculated optimal evaluations. Two conclusions can be drawn from this:

In the case for O.P. 0, the spatial resolution was increased by a factor of 2 at the expense of a slight decrease in valid detection probability. This decrease is acceptable since the resulting VDP is still within the 90-95% range. The reasoning behind this is that since velocities at that operation point are small, the dynamic velocity range loses importance, allowing the spatial range to increase.

On the other hand, O.P. 5 experienced the opposing effect. Velocities at this operation point are high therefore limiting the increase in spatial resolution since the dynamic velocity range gains importance. For this, the resolution for the evaluation was lowered (mostly in vertical direction), allowing for a larger DVR value. This results in a VDP within the acceptable range.

The standard and calculated optimal resulting VDPs for all operation points can be seen in Figure 4.24 alongside the additional resulting VDPs for O.P.'s 0 and 5.

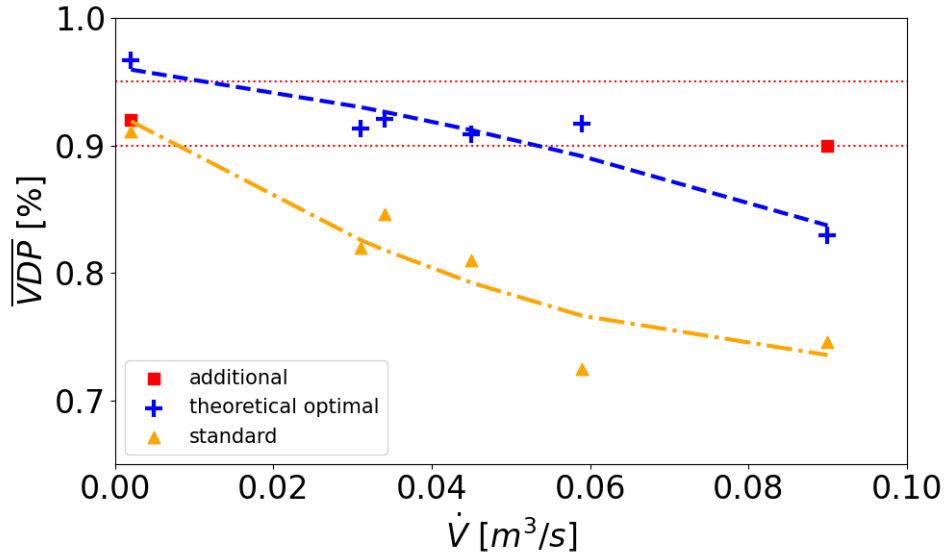


Figure 4.24: Resulting average valid detection probabilities for standard (orange triangles) and calculated optimal (blue crosses) evaluations with a best fitting curve. Additional resulting VDPs for evaluations run for operation points not satisfying the desirable VDP range are plotted as well (red squares).

To conclude this investigation, it can be said that the calculated optimal evaluation parameters yield quantitative- and qualitatively far better results than a standard evaluation for the test bench at hand. The calculations used to arrive at these parameters carefully balance all pertinent values towards the quality of a PIV evaluation in order to increase its resolution to the furthest extent without compromising the accuracy of its results.

5 Conclusions and Future Work

During the course of this thesis multiple investigations into the parameters of a PIV measurement for a centrifugal fan in a spiral casing were carried out. These were done with the goal of optimizing the results by increasing the evaluation resolution while maintaining an optimal measurement quality.

An investigation into the optimal image acquisition parameters was conducted. This resulted in the development of a protocol designed to choose the required exposure time delay to achieve the optimal average pixel displacement for a given volume flow rate and position inside the volute casing. The procedures described during this investigation are applicable for any given setup, despite the fact that the resulting values are specific for the investigated test bench and region of interest.

In order to increase the accuracy for the measurements, a new calibration plate was designed. Previously used calibration devices resulted in unnecessary uncertainties due to variations in the positioning for the calibration target. This also caused the calibration procedure to take more time and effort than what is necessary. The implemented plate allowed for a quicker and more precise calibration.

Multiple evaluation parameter variations were investigated throughout this work. Interrogation window dimensions based on the previously extracted optimal pixel displacements for a given operation point were calculated allowing an increase in the spatial resolution for a PIV experiment while maintaining the quality for its results. In addition, investigations into the optimal interrogation window overlap and cross-correlation algorithms were carried out. It was concluded that using a 50% overlap and a multi-grid algorithm result in the best image quality for a given measurement.

Evaluations run following the protocols described in this thesis were compared to standard evaluations over the same set of measurements. By comparing these results, it was concluded that the optimal parameters resulted in a higher image resolution evaluation quality. These comparisons were carried out for six different operation points for the given setup resulting in the same overall conclusions.

Future Work

This section describes possible future work to be carried out for the investigated test bench. Investigations mentioned in this section were not conducted through the duration of this work for multiple reasons including the investigation scope and time constraints.

The extent for this thesis covered mostly the investigation into acquisition and evaluation parameters for a PIV measurement. Although used and mentioned, pre-processing parameters (such as image filtering) and their effects on final results were not investigated to their full extent. An assessment into their influence, alongside the procedures explained in this work, could lead to even higher resulting image qualities. Additionally, this investigation could include the evaluation for outlier detection filters and their effects on image results and valid vector detection probabilities.

Additionally, multiple cross-correlation algorithms were compared, concluding that the use of a multi-grid algorithm yields the best results. This algorithm was not investigated to its full extent since multiple parameter variations exist for it. An investigation into the results for varying initial and final interrogation window dimensions, image pixel shift for different passes and desampling factors is worth conducting since a much better understanding can be extracted for this algorithm as well as the effect these variations have on the resulting evaluation quality.

The experimental setup used for this work is able to perform multi-plane 2D2C PIV measurements. Due to time constraints, measurements run during this thesis were done for a set z position and the procedures are therefore tailored for that position. An investigation into the variations for the parameters described in this work when using a multi-plane approach could give a better insight into the optimal acquisition and evaluation parameters when measuring across the volume for the spiral casing.

Bibliography

- Adrian, RJ (1997): *Dynamic ranges of velocity and spatial resolution of particle image velocimetry*. Measurement Science and Technology, Bd. 8, S. 1393.
- Feldle, C. (2018): *Measurements of velocity fields in a centrifugal fan by means of Particle Image Velocimetry*.
- Hain, R and Kähler, CJ (2007): *Fundamentals of multiframe particle image velocimetry (PIV)*. Experiments in fluids, Bd. 42, S. 575–587.
- Hart, Douglas P (2000): *PIV error correction*. Experiments in fluids, Bd. 29, S. 13–22.
- Keane, Richard D and Adrian, Ronald J (1991): *Optimization of particle image velocimeters: II. Multiple pulsed systems*. Measurement science and technology, Bd. 2, S. 963.
- Keller, J. (2014): *Fluid-Dynamic Fluctuations and Flow Structures in Centrifugal Pumps due to Rotor-Stator Interaction*. Doctoral thesis, Universidad de Oviedo.
- Meinhart, Carl D, Wereley, Steve T and Santiago, Juan G (1999): *PIV measurements of a microchannel flow*. Experiments in fluids, Bd. 27, S. 414–419.
- Olsen, MG and Adrian, RJ (2000): *Out-of-focus effects on particle image visibility and correlation in microscopic particle image velocimetry*. Experiments in fluids, Bd. 29, S. S166–S174.
- Pritz, Balazs, Walter, Johannes and Gabi, Martin (2018): *A Centrifugal Fan Test Bench for Validation Data at Off-Design Conditions*. In: *Proceedings of the International Conference on Fan Noise, Aerodynamics, Applications and Systems (fan2018)*, Darmstadt 2018.
- Probst, Matthias and Pritz, Balazs (2019): *Quantitative Validation of CFD-Simulation against PIV Data for a Centrifugal Fan*. In: *14th International Symposium on Experimental Computational Aerothermodynamics of Internal Flows (2019)*, Danzig, Polen, 08.07. 2019–11.07. 2019.
- Raffel, Markus, Willert, Christian E, Scarano, Fulvio, Kähler, Christian J, Wereley, Steve T and Kompenhans, Jürgen (2018): *Particle image velocimetry: a practical guide*. Springer.
- Ragni, D, Schrijer, F, Van Oudheusden, BW and Scarano, F (2011): *Particle tracer response across shocks measured by PIV*. Experiments in fluids, Bd. 50, S. 53–64.
- Shepherd, Ian C and La Fontaine, RF (1993): *Mapping the velocity field in a centrifugal fan using particle image velocimetry*. Journal of Wind Engineering and Industrial Aerodynamics, Bd. 50, S. 373–381.
- Siekmann, Helmut E and Thamsen, Paul Uwe (2013): *Strömungslehre: Grundlagen*. Springer-Verlag.
- Spurk, Joseph H. and Aksel, Nuri (2020): *Fluid Mechanics*. Springer.

- Stamhuis, Eize J (2006): *Basics and principles of particle image velocimetry (PIV) for mapping biogenic and biologically relevant flows.* Aquatic Ecology, Bd. 40, S. 463–479.
- Warner, Scott O and Smith, Barton L (2014): *Autocorrelation-based estimate of particle image density for diffraction limited particle images.* Measurement Science and Technology, Bd. 25, S. 065201.
- Yoon, Jong-Hwan and Lee, Sang-Joon (2004): *Stereoscopic PIV measurements of flow behind an isolated low-speed axial-fan.* Experimental thermal and fluid science, Bd. 28, S. 791–802.

Appendix

A.1 Optimal Image Particle Displacements for Investigated Operation Points

Operation Point 0

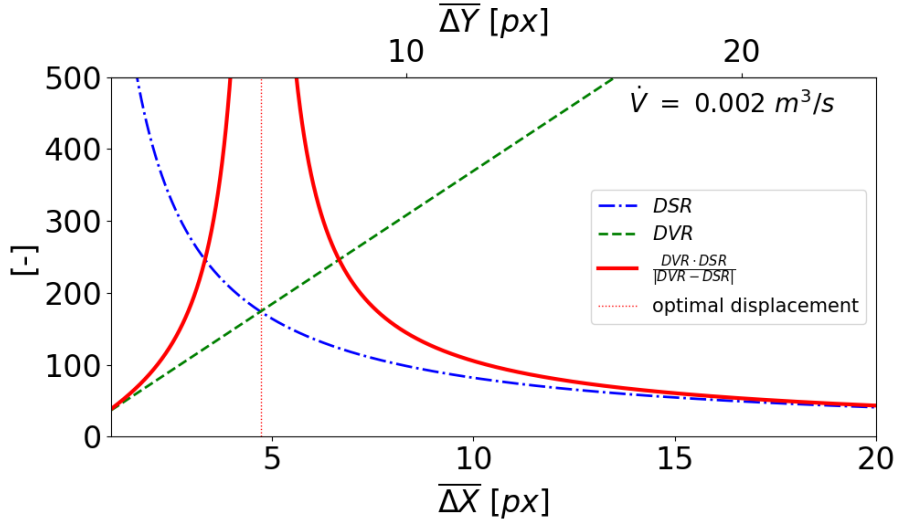


Figure A.1: Quality indicators for a given operation point with varying pixel displacements. Vertical and horizontal displacements resulting in the maximum achievable $DVR \cdot DSR / |DVR - DSR|$ ratio are marked as optimal.

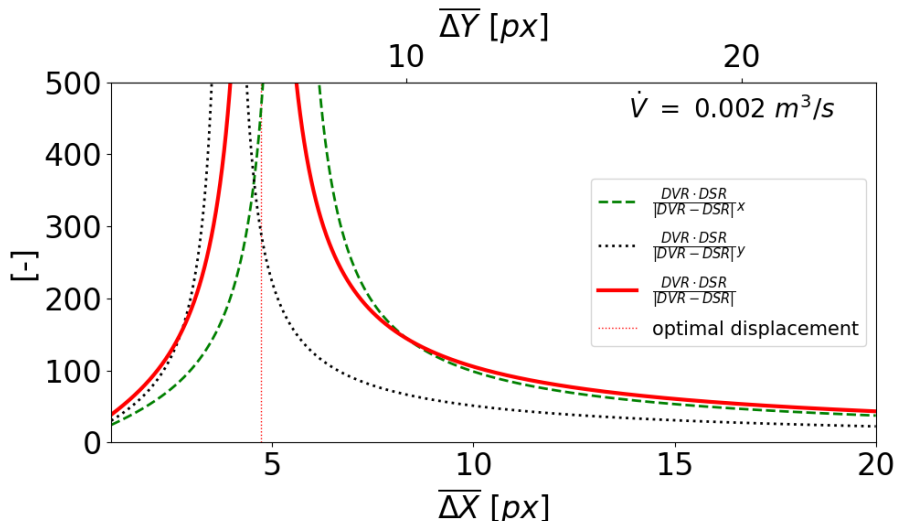


Figure A.2: Individual quality indicators for a given operation point with varying pixel displacements. Vertical and horizontal displacements resulting in the maximum achievable $DVR \cdot DSR / |DVR - DSR|$ ratio are marked as optimal.

Operation Point 1

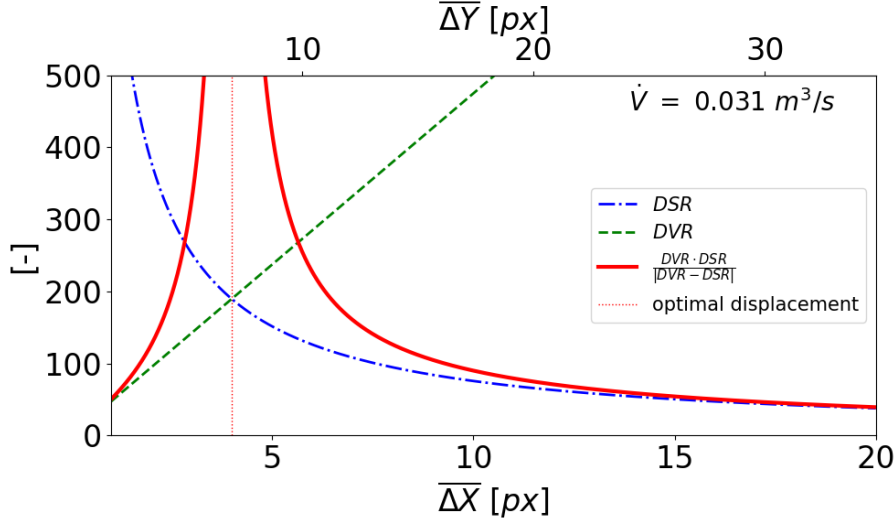


Figure A.3: Quality indicators for a given operation point with varying pixel displacements. Vertical and horizontal displacements resulting in the maximum achievable $DVR \cdot DSR / |DVR - DSR|$ ratio are marked as optimal.

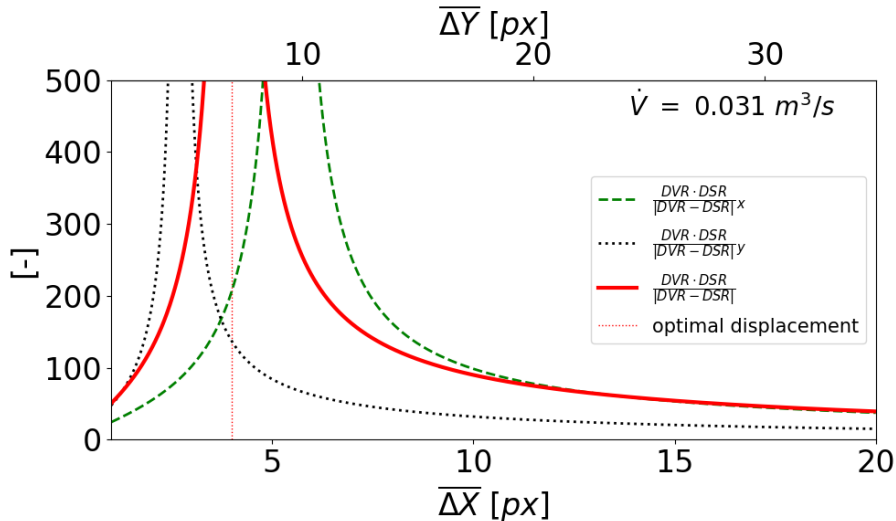


Figure A.4: Individual quality indicators for a given operation point with varying pixel displacements. Vertical and horizontal displacements resulting in the maximum achievable $DVR \cdot DSR / |DVR - DSR|$ ratio are marked as optimal.

Operation Point 3

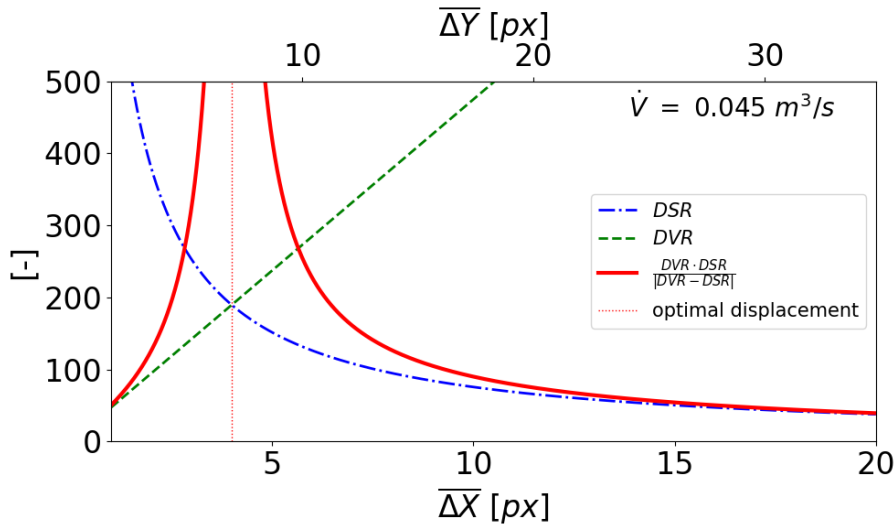


Figure A.5: Quality indicators for a given operation point with varying pixel displacements. Vertical and horizontal displacements resulting in the maximum achievable $DVR \cdot DSR / |DVR - DSR|$ ratio are marked as optimal.

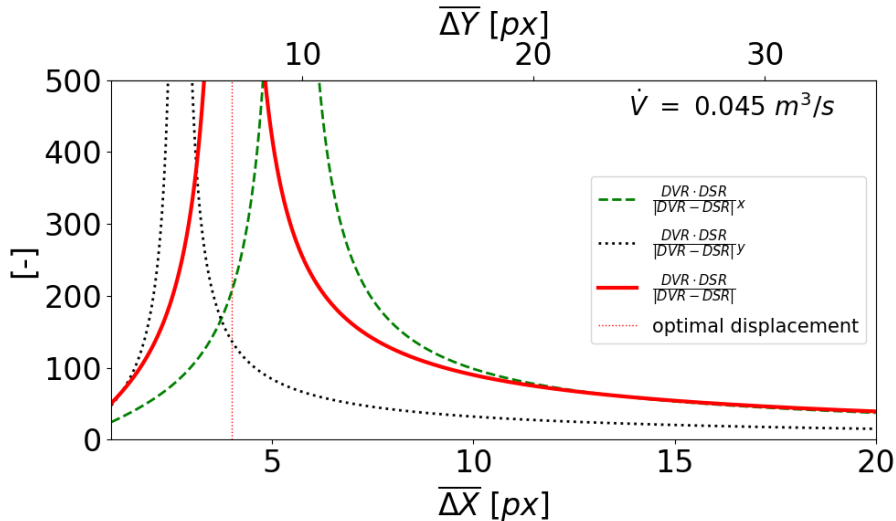


Figure A.6: Individual quality indicators for a given operation point with varying pixel displacements. Vertical and horizontal displacements resulting in the maximum achievable $DVR \cdot DSR / |DVR - DSR|$ ratio are marked as optimal.

Operation Point 4

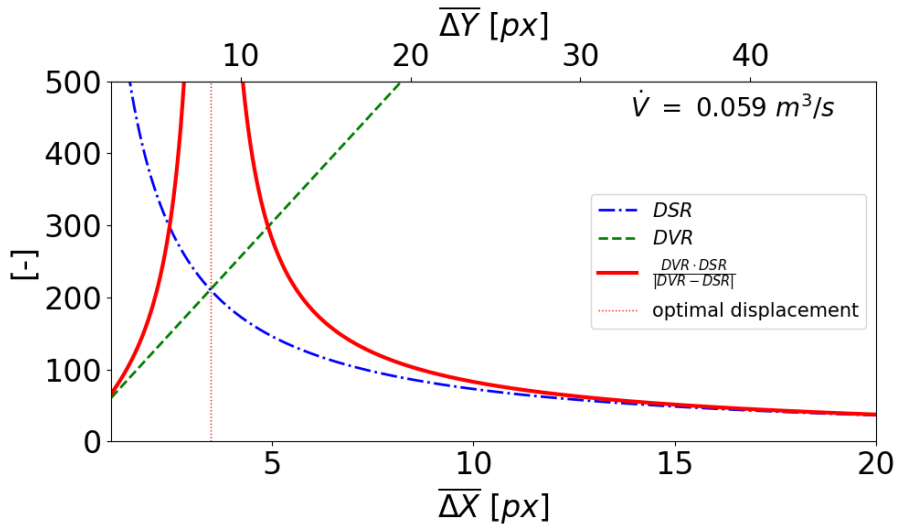


Figure A.7: Quality indicators for a given operation point with varying pixel displacements. Vertical and horizontal displacements resulting in the maximum achievable $DVR \cdot DSR/|DVR - DSR|$ ratio are marked as optimal.

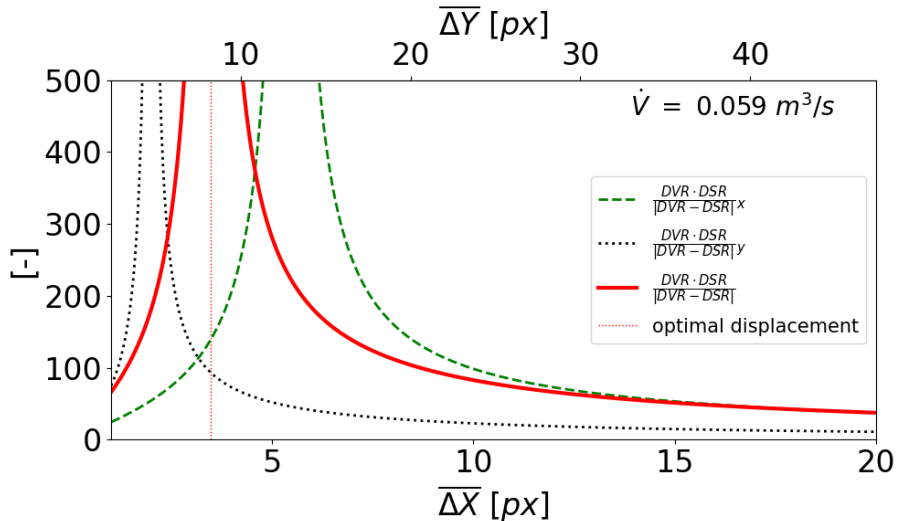


Figure A.8: Individual quality indicators for a given operation point with varying pixel displacements. Vertical and horizontal displacements resulting in the maximum achievable $DVR \cdot DSR/|DVR - DSR|$ ratio are marked as optimal.

Operation Point 5

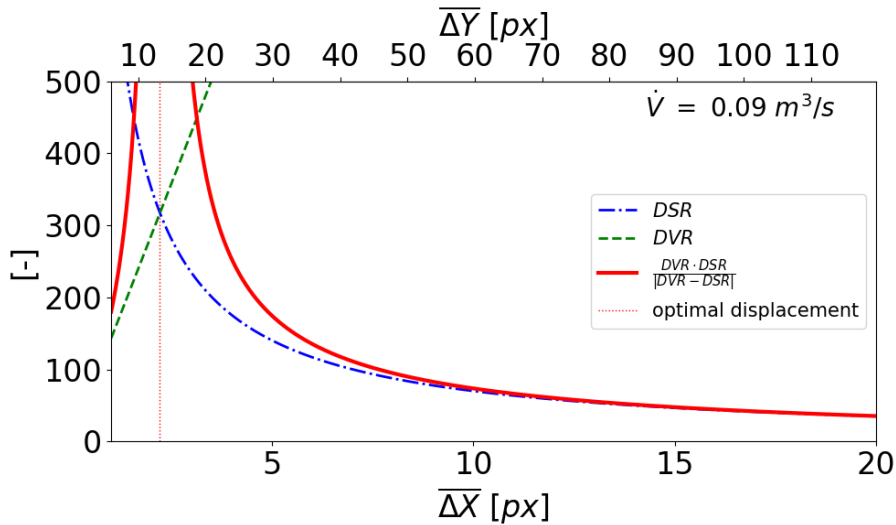


Figure A.9: Quality indicators for a given operation point with varying pixel displacements. Vertical and horizontal displacements resulting in the maximum achievable $DVR \cdot DSR / |DVR - DSR|$ ratio are marked as optimal.

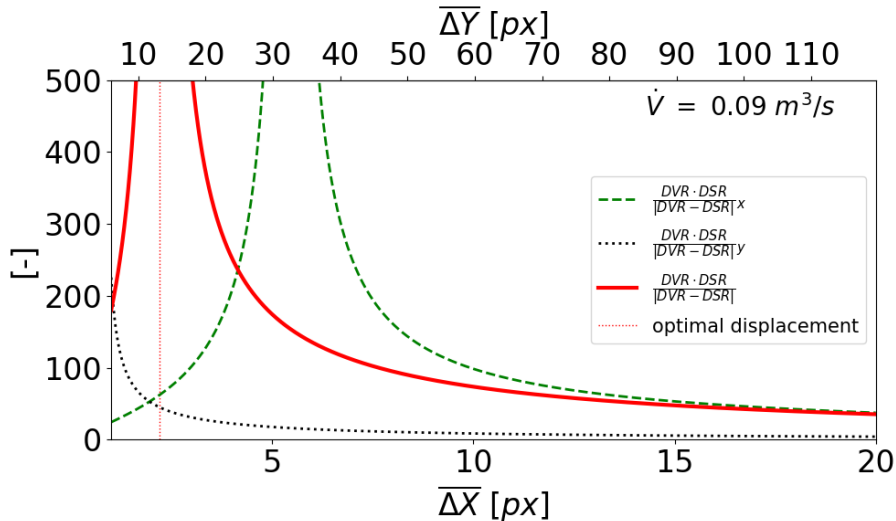


Figure A.10: Individual quality indicators for a given operation point with varying pixel displacements. Vertical and horizontal displacements resulting in the maximum achievable $DVR \cdot DSR / |DVR - DSR|$ ratio are marked as optimal.

A.2 Resulting Figures for Investigated Operation Points

Operation Point 0

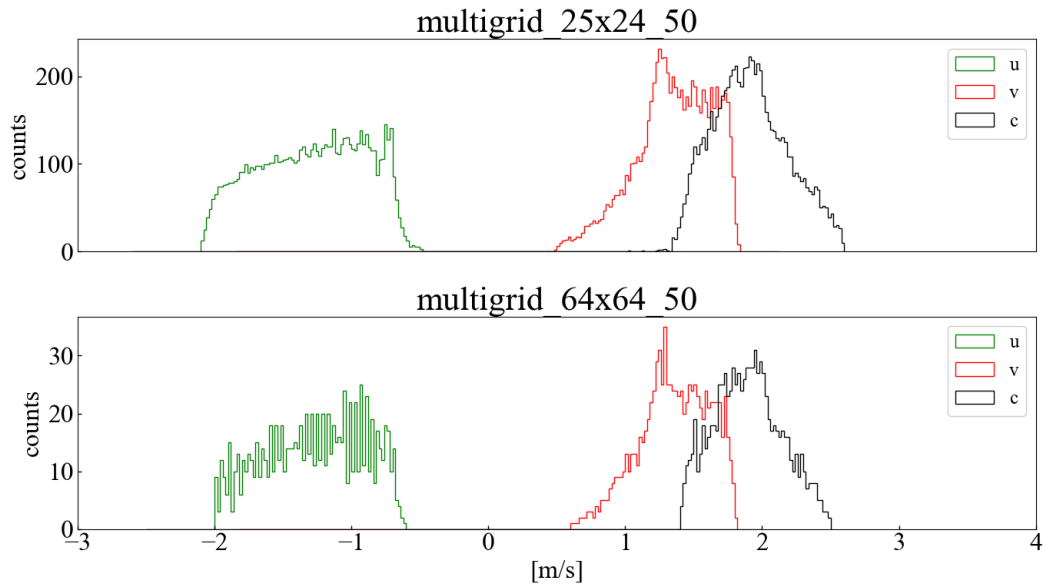


Figure A.11: Histogram for velocity components for optimal and standard evaluations.

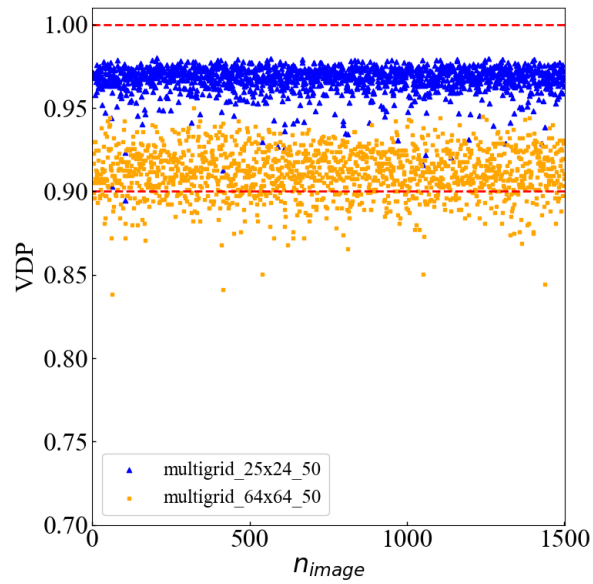


Figure A.12: Valid detection probabilities (VDP) for optimal and standard evaluations.

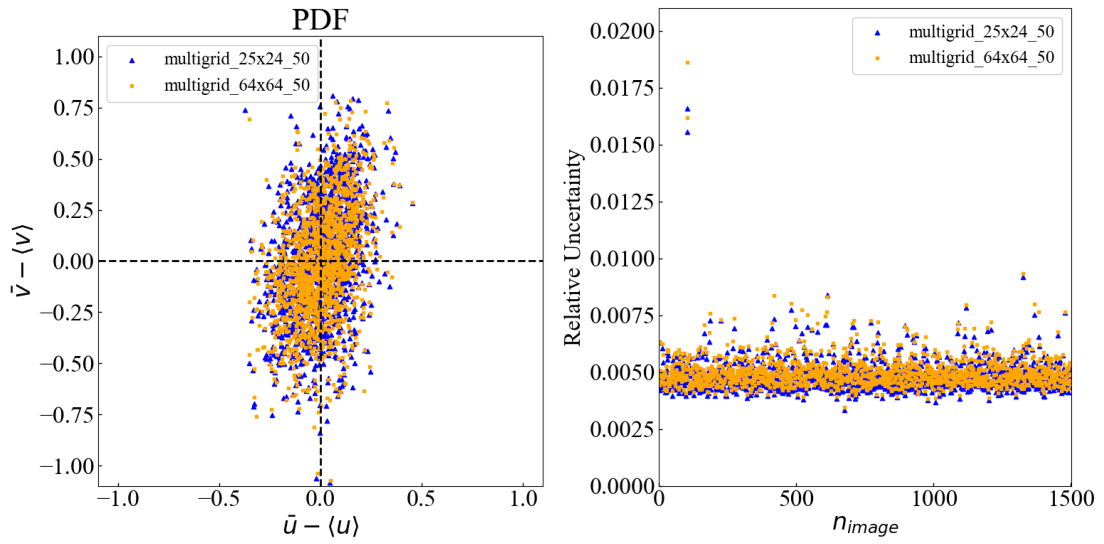


Figure A.13: Displacement scatter plots (left) and relative uncertainties (right) for optimal and standard evaluations.

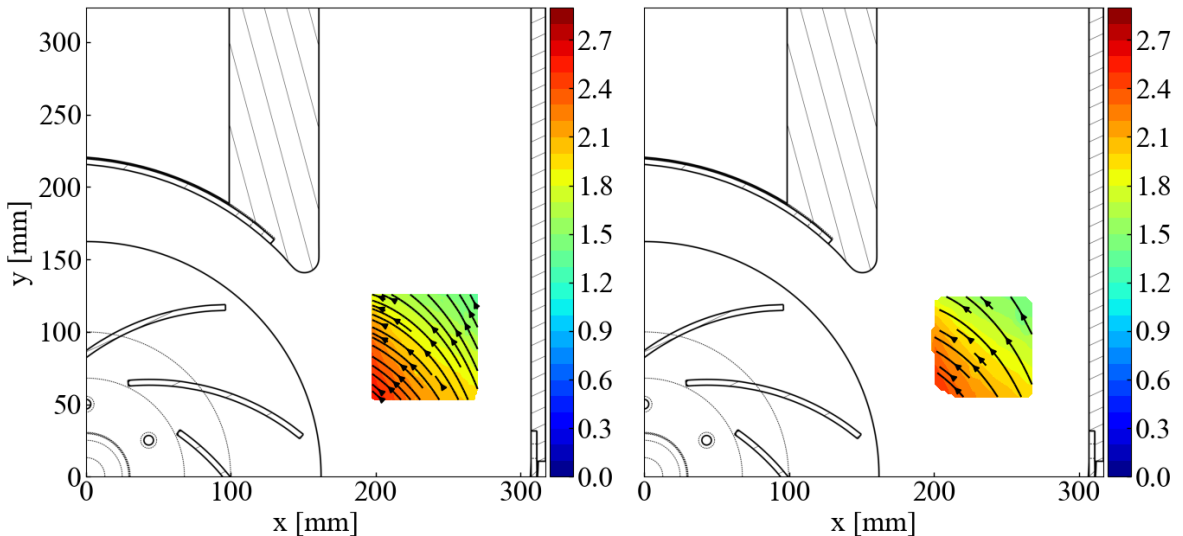


Figure A.14: Contour plots inside the area of interest in the spiral casing for the optimal evaluation (left) and standard evaluation (right).

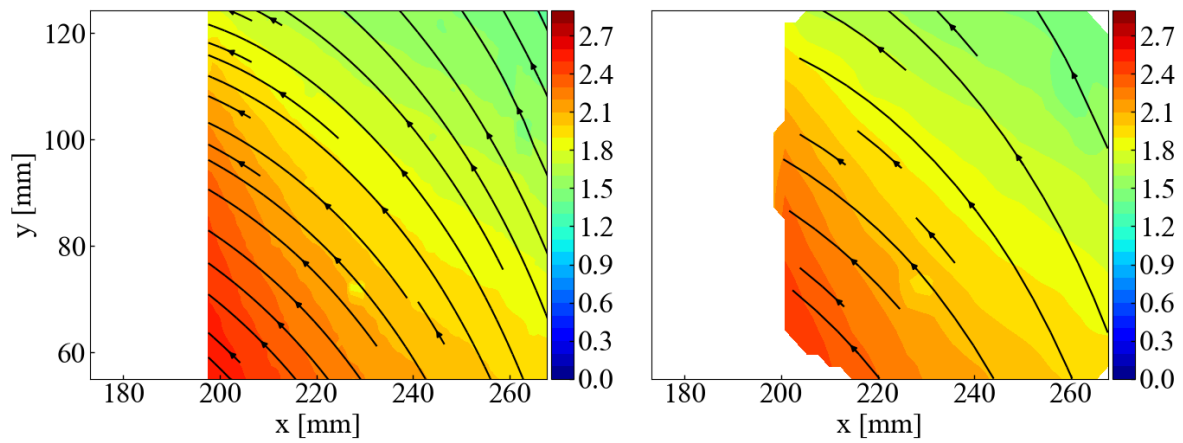


Figure A.15: Contour plots for the optimal evaluation (left) and standard evaluation (right).
White spaces represent masked areas.

Operation Point 1

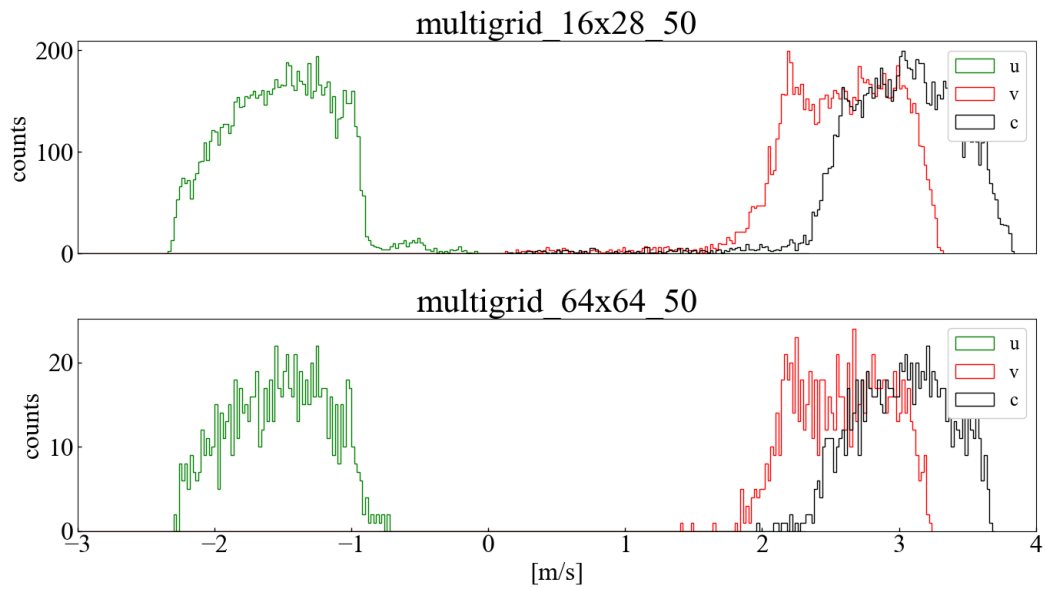


Figure A.16: Histogram for velocity components for optimal and standard evaluations.

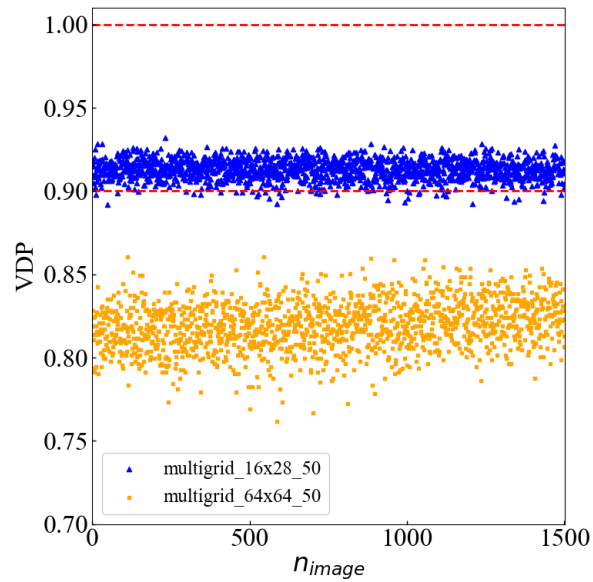


Figure A.17: Valid detection probabilities (VDP) for optimal and standard evaluations.

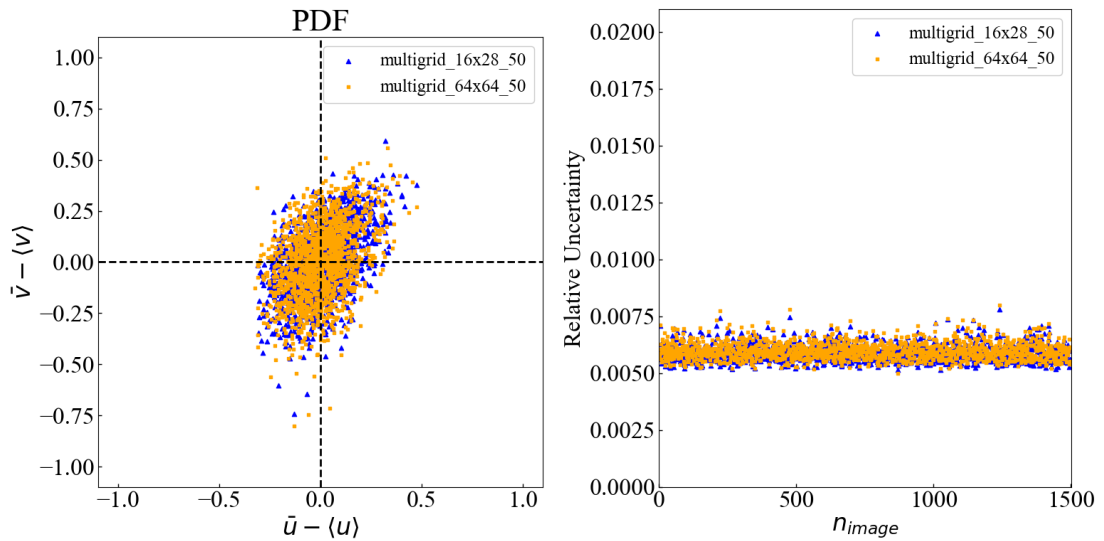


Figure A.18: Displacement scatter plots (left) and relative uncertainties (right) for optimal and standard evaluations.

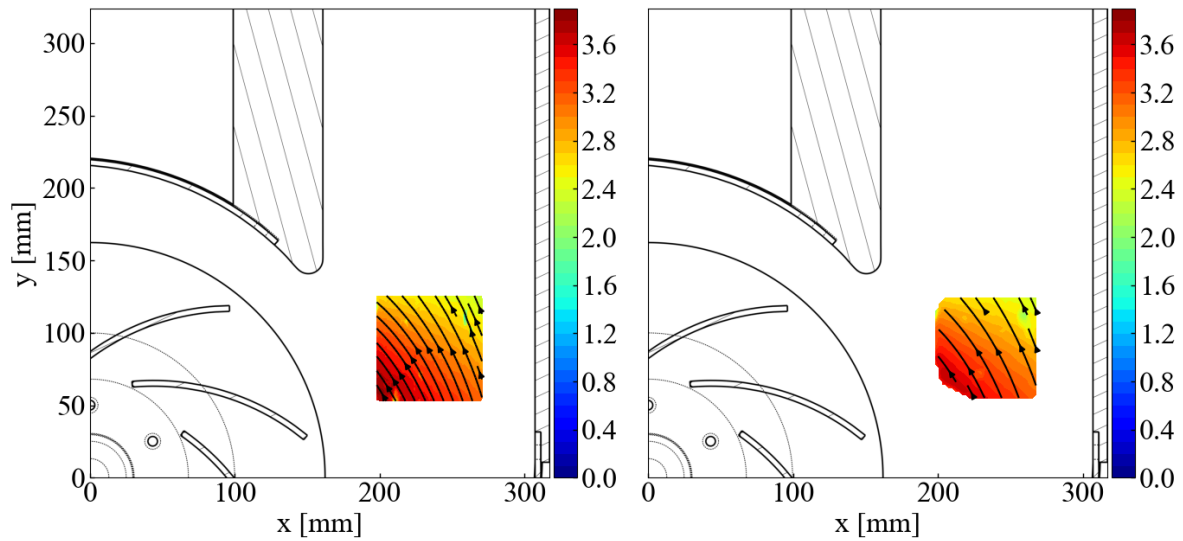


Figure A.19: Contour plots inside the area of interest in the spiral casing for the optimal evaluation (left) and standard evaluation (right).

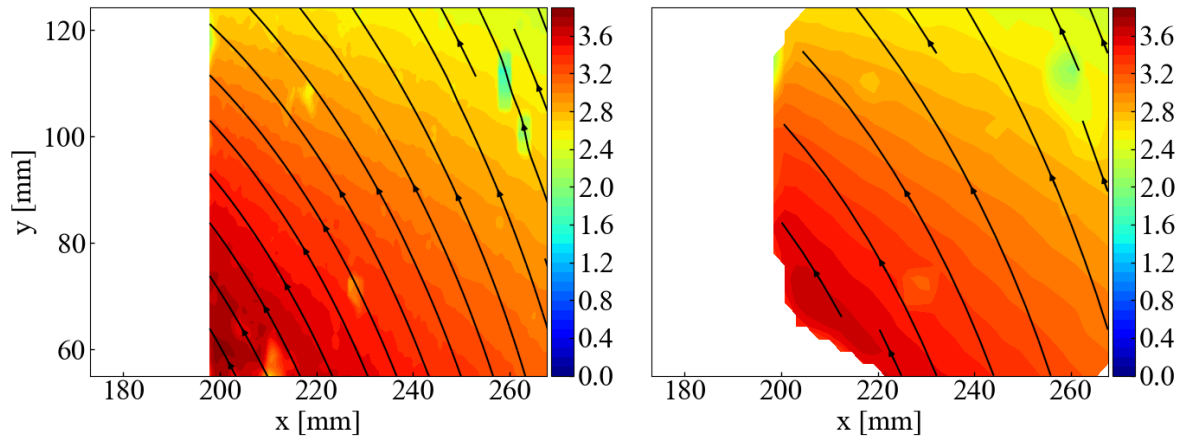


Figure A.20: Contour plots for the optimal evaluation (left) and standard evaluation (right). White spaces represent masked areas.

Operation Point 3

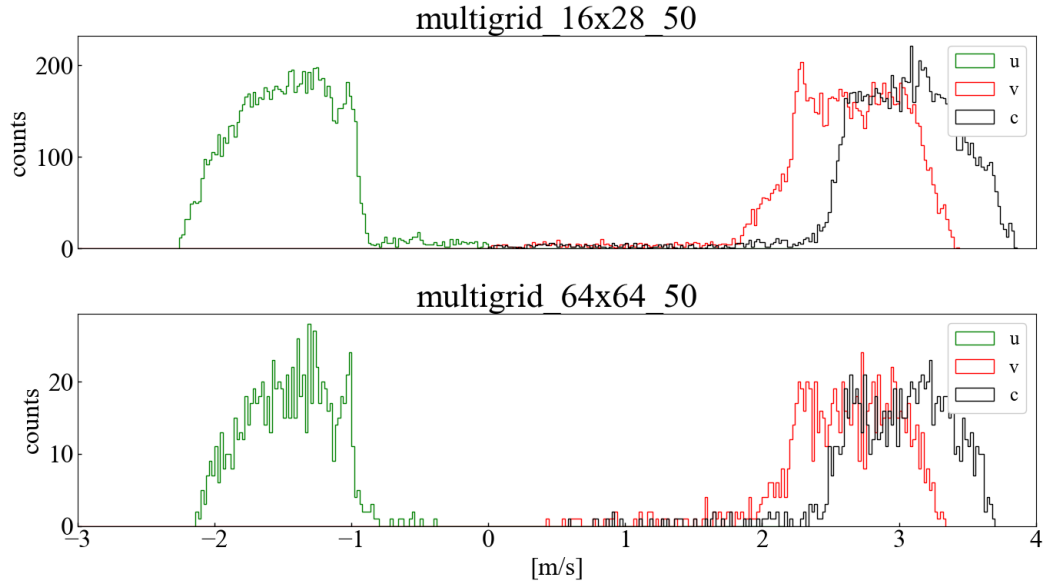


Figure A.21: Histogram for velocity components for optimal and standard evaluations.

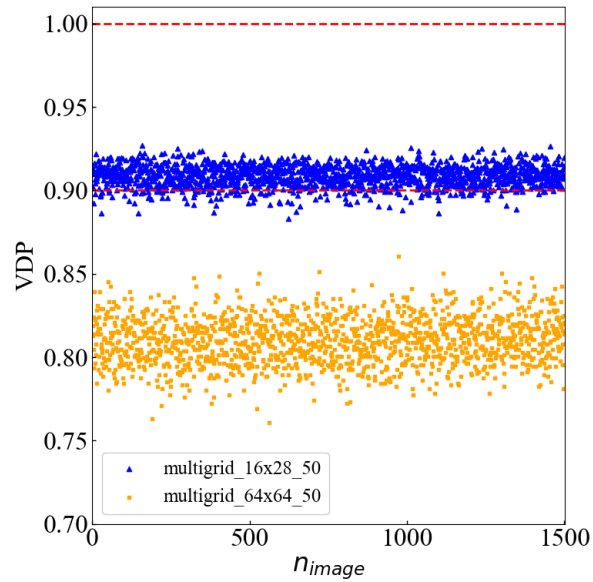


Figure A.22: Valid detection probabilities (VDP) for optimal and standard evaluations.

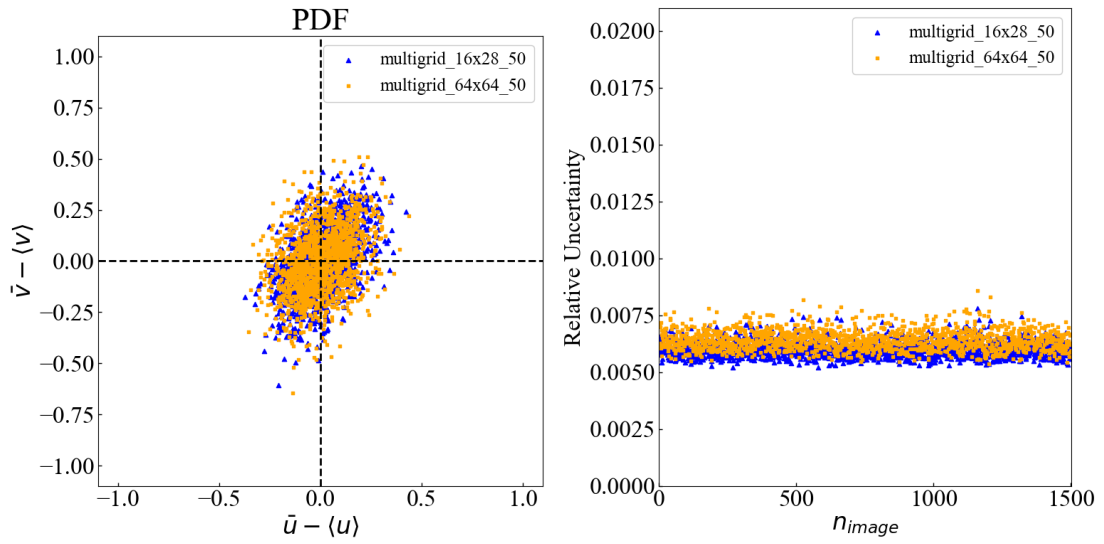


Figure A.23: Displacement scatter plots (left) and relative uncertainties (right) for optimal and standard evaluations.

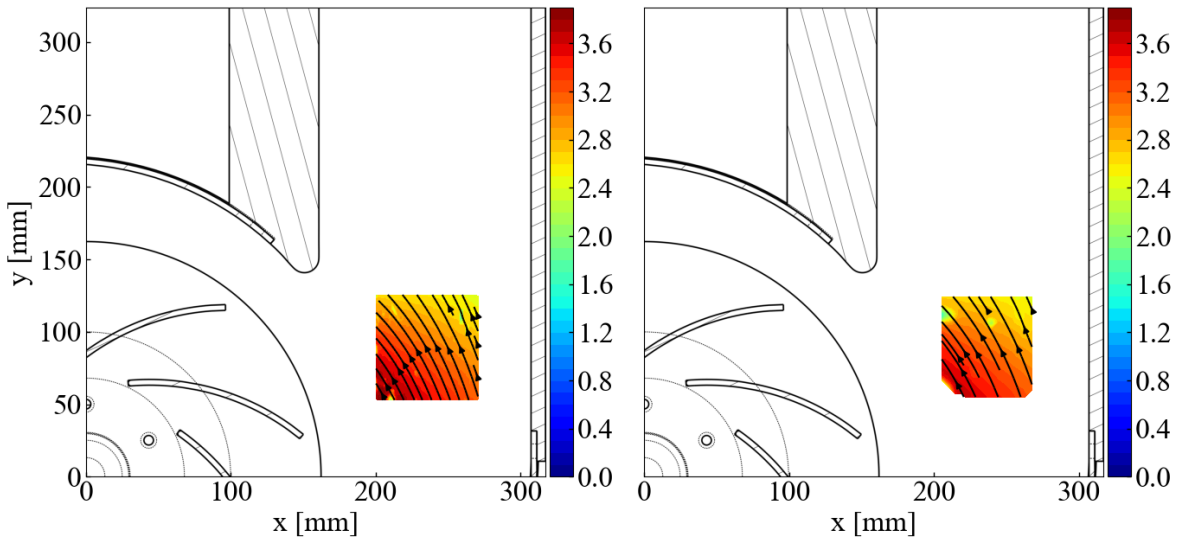


Figure A.24: Contour plots inside the area of interest in the spiral casing for the optimal evaluation (left) and standard evaluation (right).

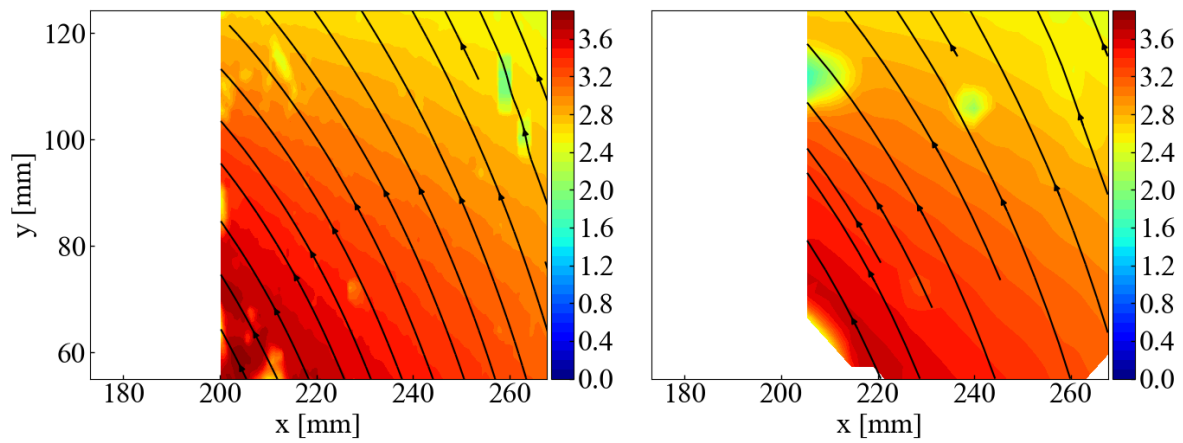


Figure A.25: Contour plots for the optimal evaluation (left) and standard evaluation (right).
White spaces represent masked areas.

Operation Point 4

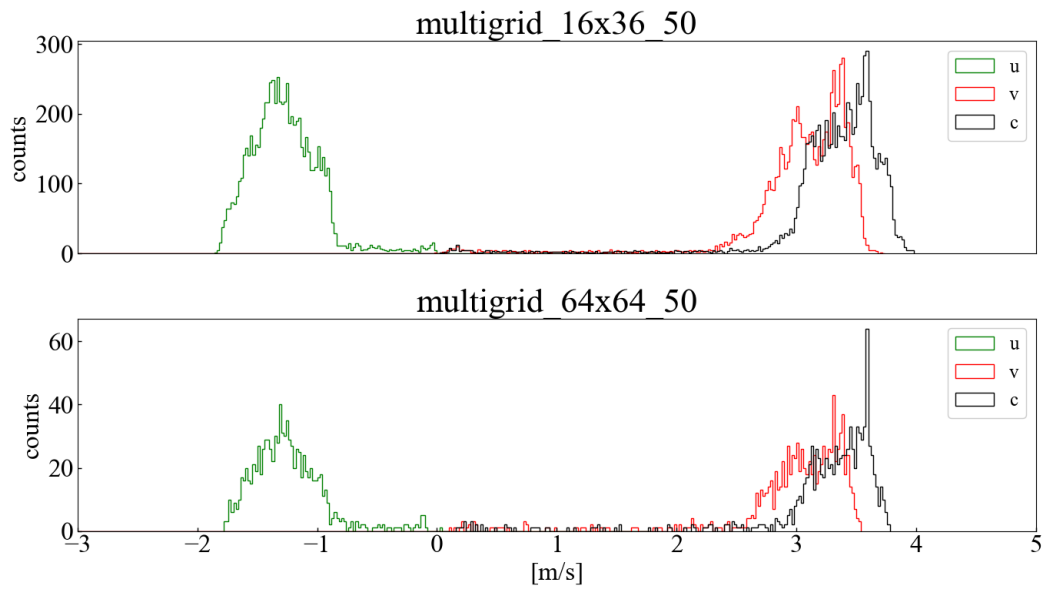


Figure A.26: Histogram for velocity components for optimal and standard evaluations.

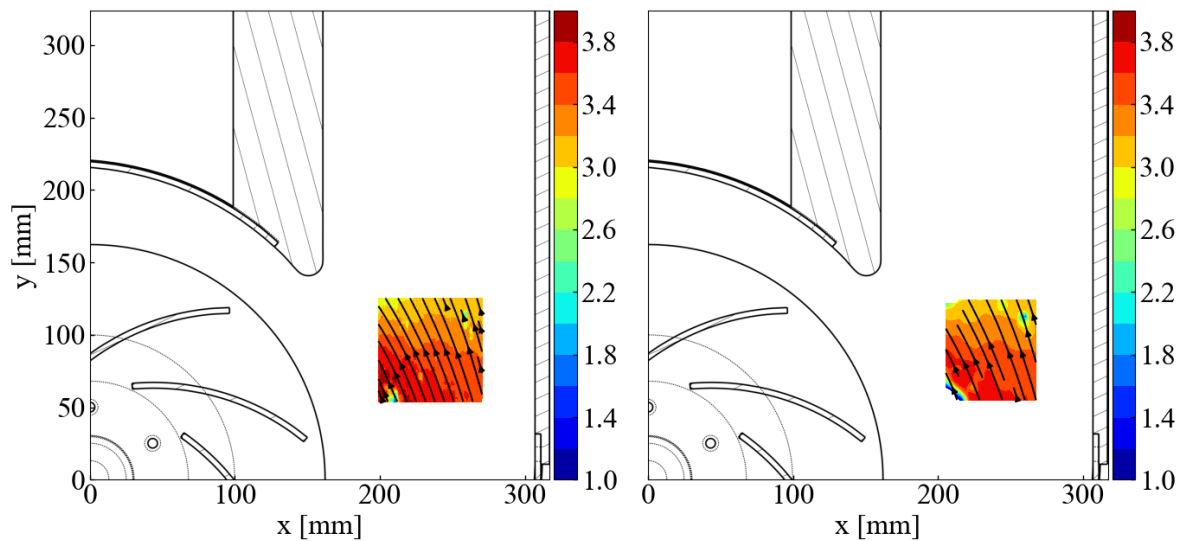


Figure A.27: Contour plots inside the area of interest in the spiral casing for the optimal evaluation (left) and standard evaluation (right).

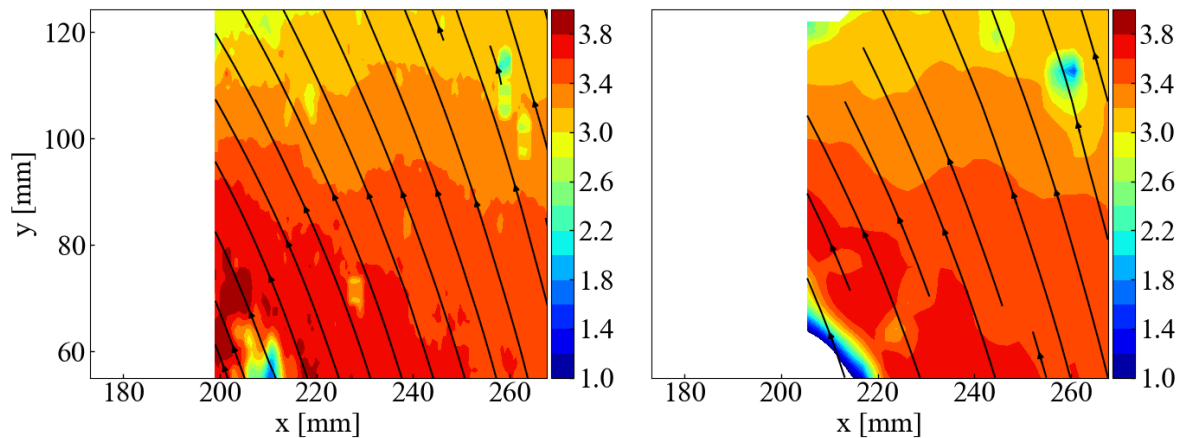


Figure A.28: Contour plots for the optimal evaluation (left) and standard evaluation (right). White spaces represent masked areas.

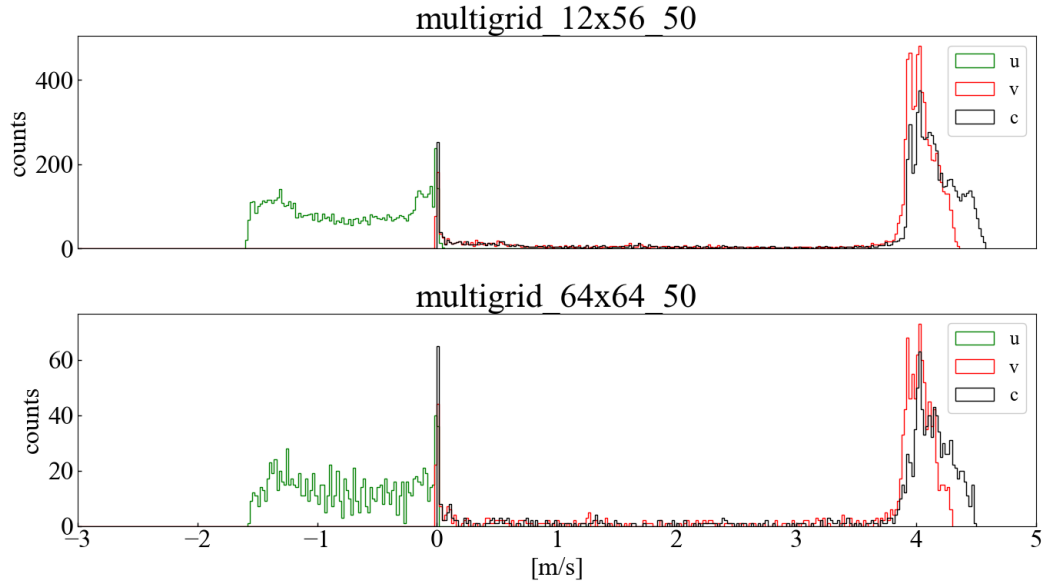
Operation Point 5

Figure A.29: Histogram for velocity components for optimal and standard evaluations.

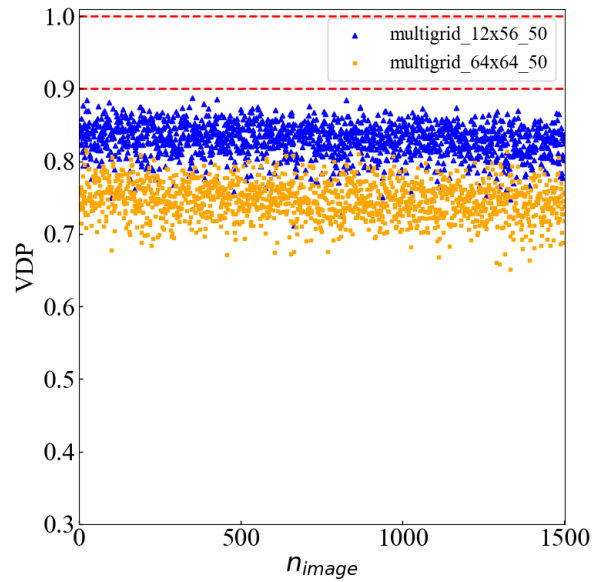


Figure A.30: Valid detection probabilities (VDP) for optimal and standard evaluations.

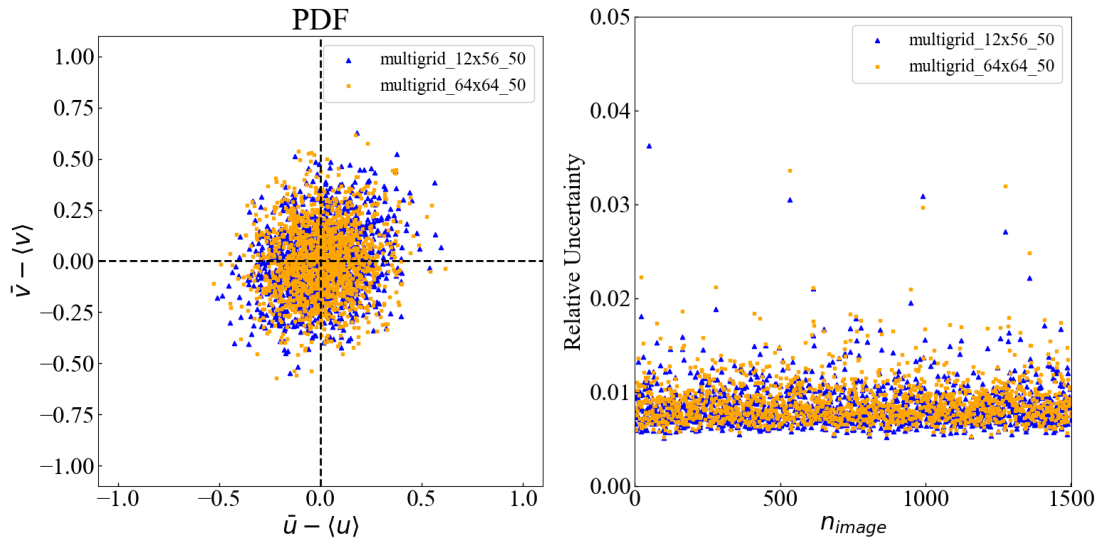


Figure A.31: Displacement scatter plots (left) and relative uncertainties (right) for optimal and standard evaluations.

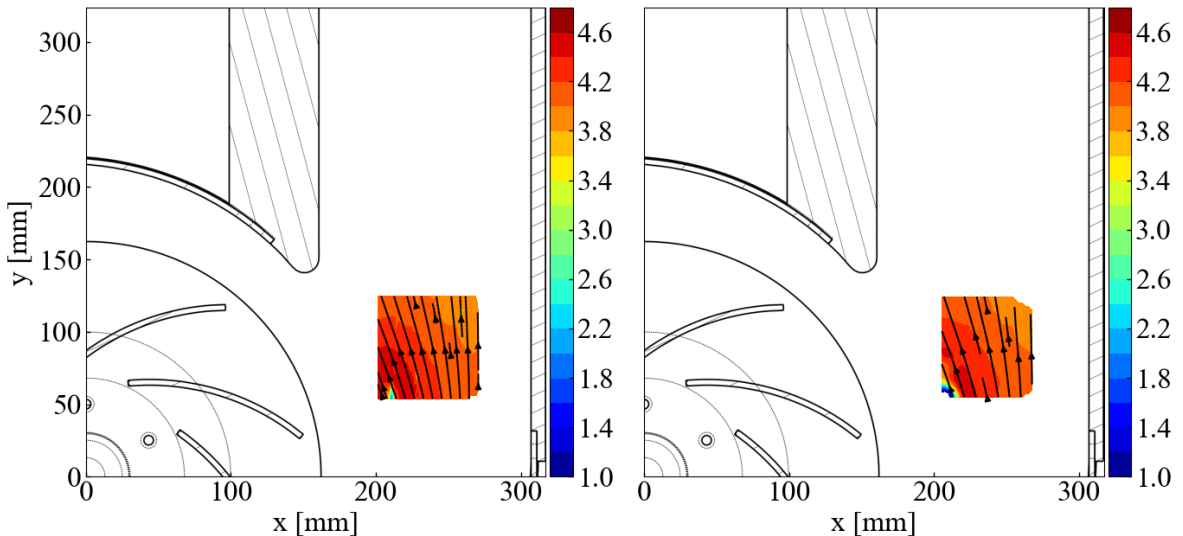


Figure A.32: Contour plots inside the area of interest in the spiral casing for the optimal evaluation (left) and standard evaluation (right).

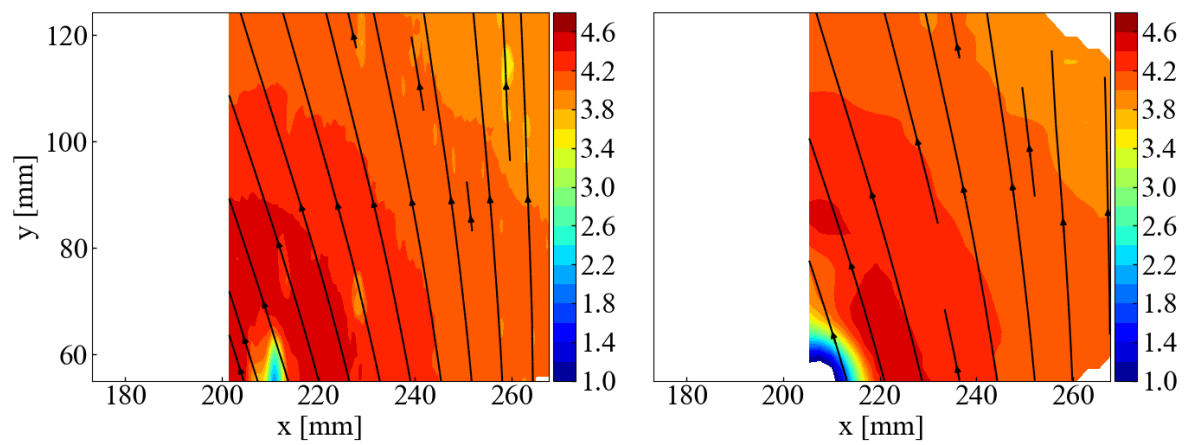


Figure A.33: Contour plots for the optimal evaluation (left) and standard evaluation (right).
White spaces represent masked areas.